RESEARCH ARTICLE

Key Points:
- Generating cells at the top of midlevel mixed-phase clouds are commonly observed over the high-latitude Southern Ocean
- Supercooled drizzle is present in two of the three cases examined here with phase changes following supercooled liquid layer seeding
- Seeding of single-layer ice-precipitating supercooled liquid clouds occurs in the trailing clouds of each system

Correspondence to:
S. P. Alexander,
simon.alexander@aad.gov.au

Mixed-Phase Clouds and Precipitation in Southern Ocean Cyclones and Cloud Systems Observed Poleward of 64°S by Ship-Based Cloud Radar and Lidar

S. P. Alexander[1,2] , G. M. McFarquhar[3] , R. Marchand[4] , A. Protat[2,5] , É. Vignon[6,7] , G. G. Mace[8] , and A. R. Klekociuk[1,2]

[1]Australian Antarctic Division, Kingston, TAS, Australia, [2]Australian Antarctic Program Partnership, Institute for Marine and Antarctic Studies, University of Tasmania, Hobart, TAS, Australia, [3]Cooperative Institute for Mesoscale Meteorological Studies and the School of Meteorology, University of Oklahoma, Norman, OK, USA, [4]Department of Atmospheric Sciences, University of Washington, Seattle, WA, USA, [5]Bureau of Meteorology, Melbourne, VIC, Australia, [6]Environmental Remote Sensing Laboratory (LTE), École Polytechnique Fédérale de Lausanne (EPFL), Lausanne, Switzerland, [7]Laboratoire de Météorologie Dynamique IPSL, Sorbone Universités, CNRS, Paris, France, [8]Department of Atmospheric Sciences, University of Utah, Salt Lake City, UT, USA

Abstract Mixed-phase clouds (MPCs), composed of both liquid and ice, are prevalent in Southern Ocean cyclones. A characterization of these clouds on fine vertical scales is required in order to understand the microphysical processes within these clouds, and for model and satellite evaluations over this region. We investigated three examples of cloud systems collected by ship-mounted remote-sensing instruments adjacent to East Antarctica at latitudes between 64°S and 69°S. These cases allow us to examine the properties of midlevel MPCs, with cloud tops between 2 and 6 km. Midlevel MPCs contain multiple layers of supercooled liquid water (SLW) embedded within ice during the passage of cyclones. SLW layers are capped by strong temperature inversions and are observed at temperatures as low as $-31°C$. Convective generating cells (GCs) are present inside supercooled liquid-topped midlevel MPCs. The horizontal extent, vertical extent, and maximum upward Doppler velocity of these GCs were 0.6–3.6 km, 0.7–1.0 km, and 0.5–1.0 m s^{-1}, respectively, and are consistent with observations from previous lower-latitude studies. Ice precipitation is nearly ubiquitous, except in the thinnest clouds at the trailing end of the observed systems. Seeding of lower SLW layers from above leads to periods with either larger ice particles or greater ice precipitation rates. Periods of supercooled drizzle lasting up to 2 h were observed toward the end of two of the three cyclone systems. This supercooled drizzle turns into predominantly ice precipitation as the result of seeding by ice clouds located above the precipitating SLW layer.

1. Introduction

Mixed-phase clouds (MPCs) containing both ice and liquid occur commonly from the tropics to the polar regions (e.g., Hogan et al., 2003; Hu et al., 2010; McFarquhar et al., 2007; Mioche et al., 2015). These clouds remain difficult to model correctly due to the interplay of microphysical and dynamical processes which regulate their formation, maintenance, and decay (Sotiropoulou et al., 2016), and because the scales over which these processes occur are substantially smaller than the resolution of climate and weather prediction models. The observed longevity of MPCs indicates that the removal of ice crystals from the cloud through gravitational sedimentation must be balanced by a continuous source of liquid water. Intracloud processes including updrafts and turbulent mixing, or a continuous supply of new liquid at cloud base, must be sufficient to replenish the liquid water (Korolev & Field, 2008; Rauber & Tokay, 1991). The correct modeling of cloud phase partitioning between ice and liquid water is necessary to match observations of reflected short-wave radiation (Forbes & Ahlgrimm, 2014; Kay et al., 2016; Lenaerts et al., 2017; Tan et al., 2016). Cloud phase was recently shown to strongly influence Antarctic ice shelf surface melting (Gilbert et al., 2020). The presence of multilayered MPCs reported in the extratropics indicates that these clouds can exist and persist in a complex environment (Verlinde et al., 2013). Initiation of upper (or free-tropospheric) MPC layers are often due to large-scale advection of moisture, while MPC layers closer to the surface are also influenced by surface processes such as heat and moisture fluxes and turbulence (Luo et al., 2008).

The upper part of an idealized midlevel MPC (which we refer to here as being those clouds with tops between 2- and 6-km altitude and temperatures between −10°C and −30°C) often consists of a thin supercooled liquid water (SLW) layer of thickness less than about 300 m (Ansmann et al., 2009; Barrett et al., 2020; Hogan et al., 2003), beneath which supercooled drizzle and/or ice precipitation may be present. The depth of this precipitating layer depends upon the depth of ice supersaturation but is usually much greater than the thickness of the SLW layer itself (Rauber & Tokay, 1991). The liquid nature of these cloud tops results in strong radiative cooling by reflecting incoming shortwave radiation and emitting longwave radiation (Heymsfield et al., 1991; Hogan et al., 2003). The longwave emission produces strong cooling at cloud top that initiates turbulent mixing driven by the negatively buoyant air parcels and a large temperature inversion is observed at cloud top height due to this turbulent mixing and radiative cooling. Ice particles are formed inside the liquid layer through heterogeneous freezing and secondary ice production processes and grow rapidly by vapor deposition, riming, and aggregation. Another temperature inversion may be evident at the base of the ice virga layer due to latent cooling as the ice particles sublimate in a drier air mass (Forbes & Hogan, 2006). It remains unclear whether this idealized description is applicable to MPCs found over the Southern Ocean and coastal Antarctica due to a lack of observational data.

MPCs are present throughout the lifecycle of extratropical cyclones, both within ice clouds (of several kilometers vertical extent) and in postfrontal boundary-layer clouds (Field et al., 2004; Jackson et al., 2012; Noh et al., 2019). Generating cells (GCs) and their associated fall streaks occur frequently within extratropical cyclones and are important for understanding surface precipitation due to their role in ice production (Cunningham & Yuter, 2014; Keppas et al., 2018; Kumjian et al., 2014; Plummer et al., 2015). These GCs are small regions of convection located at or near cloud top, and exhibit relatively large updraft speeds (of the order of 1–2 m s^{-1}), and a confined vertical and horizontal extent (1–2 km and less than a few kilometers, respectively) (Rosenow et al., 2014). These GC characteristics are consistent between cyclones, but on the other hand the temperature and altitude at which GCs occur can vary markedly (Kumjian et al., 2014). Aircraft observations of generating cells over the Southern Ocean (between 43°S and 61°S) revealed a mean horizontal scale of around 400 m (Wang et al., 2020), which is lower than mean Northern Hemisphere GC scales.

Satellite and surface-based observations suggest that SLW clouds and low-altitude SLW-topped MPCs are particularly common in the Southern Ocean compared to other regions of the world (Ceppi et al., 2016; Choi et al., 2014; Hu et al., 2010; Huang et al., 2012; Kanitz et al., 2011; Marchand et al., 2009; Morrison et al., 2011; Storelvmo et al., 2015), and are likely more common than above oceans in the Northern Hemisphere at similar latitudes (Ceppi et al., 2016; Choi et al., 2014; Huang et al., 2014; McCoy et al., 2014). This may be due to the relatively low ice nucleating particle (INP) concentration in this region (Burrows et al., 2013; McCluskey et al., 2018), which inhibits primary ice production within the clouds and could restrict precipitation. The ubiquity of low-level cloud over the Southern Ocean (Haynes et al., 2011; Marchand et al., 2009) makes understanding boundary-layer cloud processes and microphysics from space challenging, because satellite-based products suffer from phase uncertainty beneath cloud top height, especially in the presence of multiple cloud decks (Mace, 2010). Surface-based remote-sensing and in situ observations are therefore required to quantify cloud properties and complement the satellite observations (Listowski et al., 2019). Recent campaigns have begun to address the paucity of these data over the Southern Ocean by employing aircraft (Chubb et al., 2013; Huang et al., 2015) and ship-based platforms (Alexander & Protat, 2019; Klekociuk et al., 2020; Kuma et al., 2020; Mace & Protat, 2018a; Protat et al., 2017) to quantify cloud, aerosol, and precipitation properties, and evaluate models and satellite retrievals.

Although characterization of MPCs in the Arctic using surface-based active remote sensors is further advanced than at high Southern latitudes (e.g., Morrison et al., 2012; Verlinde et al., 2013), it is unlikely that the results from the Arctic are translatable to the Southern Ocean and coastal Antarctic region due to differences in aerosol concentrations, meteorology, and surface forcing. The Southern Ocean is characterized by strong surface winds and the continuous passage of extratropical cyclones and associated frontal cloud systems throughout the year. The winds experienced along and adjacent to much of coastal East Antarctica are a mixture of local katabatic forcing from the interior of the continent, and intermittent strong northeasterly winds associated with the passage of warm fronts from the cyclones centered in the storm track further north (Alexander et al., 2017; Orr et al., 2014; Turner et al., 2009). Correct cloud phase representation is

Table 1
MARCUS Instrumentation and Their Data Used in the Present Study

Instrument	Observed or derived parameters used
Marine W-band Cloud Radar (MWACR)	Reflectivity, Doppler velocity
Micropulse lidar (MPL)	Backscatter, depolarization ratio, cloud extent, cloud phase
Radiosondes	Temperature, humidity, wind velocities
Backscatter radar wind profiler (BSRWP)	Horizontal wind velocities
2-Channel microwave radiometer (MWR)	Liquid water path, precipitable water vapor

also necessary for correctly modeling snow melting along the Antarctic coastline (Gilbert et al., 2020; King et al., 2015).

In this study, we examine aspects of clouds and precipitation in three extratropical systems which were located close to the East Antarctic coastline. The clouds in the warm and cold sectors of two cyclone passages are examined for two of these cases, while the third case is an example of an extensive cloud system formed in the presence of a weak trough. We use observations collected by a suite of instruments deployed aboard an icebreaking ship during the Measurements of Aerosols, Radiation, and Clouds over the Southern Oceans (MARCUS) campaign to determine characteristics of generating cells, mixed-phase cloud occurrence, and precipitation phase. Such characterization, and the identification of the synoptic-scale forcings and the thermodynamic environment in which MPCs exist, is necessary if we are to understand their presence, prevalence, evolution, and endurance over this near-coastal region. Section 2 describes the data used. We examine the three systems in detail in Section 3, including their generating cells and precipitation phase. The results are then discussed and related to prior observations in Section 4 before the conclusions in Section 5.

2. Data and Analysis

The MARCUS project installed instruments from the DoE Atmospheric Radiation Measurements (ARM) Mobile Facility 2 (AMF2) aboard the Australian icebreaking vessel *RSV Aurora Australis* between November 2017 and March 2018 (McFarquhar et al., 2021). A comprehensive suite of instrumentation collected data during three transits between Australia and Antarctica, and one between Australia and Macquarie Island, during the summer season. The MARCUS instrumentation used in the present study is summarized in Table 1.

All data analyzed in this study were acquired during the third *RSV Aurora Australis* voyage (V3) of the summer season. MWACR data are calibrated by adding 4.5 dB to the reflectivity profiles provided by ARM. This value was deduced from evaluations of the MARCUS MWACR reflectivity against the calibrated W-band cloud radar onboard the CAPRICORN-II voyage over similar latitudes and times (Mace et al., 2021), and is consistent with the ARM cloud radar offsets identified by Kollias et al. (2019). The MWACR was mounted on a stabilizing platform which helped ensure that it remained vertically pointing, although as we will detail below, the ship's heave, pitch, and roll during the three case studies was minimal.

Raw 532 nm backscatter return signals from the MPL are processed to remove background noise, corrected for beam overlap, and are then calibrated using lidar signal from aerosol-free regions above the boundary layer, following Alexander and Protat (2018). Cloud base and vertical extent (up to the limit of lidar signal attenuation) are calculated from the calibrated backscatter and depolarization ratio profiles following the return signal gradient algorithm described in Wang and Sassen (2001). Uncertainty in cloud base height is due to the inherently noisy nature of the backscatter gradients, which is reduced by vertically smoothing the backscatter profiles with a five-point smoothing function. This smoothing is performed prior to determining the maximum gradient in backscatter, which we assign to be the cloud base height. Cloud phase is determined using the results from Hu et al. (2010), including accounting for horizontally oriented ice plates because the MPL points vertically. We first determine cloud base height, vertical extent, and phase of those clouds which exceed a large backscatter gradient threshold at cloud base (note that there is little sensitivity to the actual threshold value set). These clouds are predominantly, but not exclusively, liquid water. We then separately calculate cloud base height, vertical extent, and phase of clouds which have small backscatter
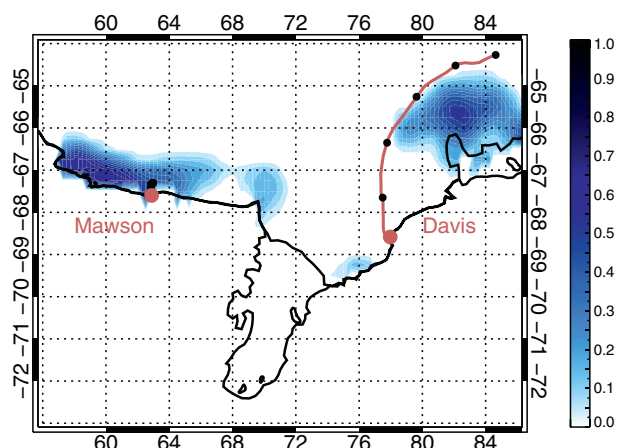
Figure 1. The East Antarctic region of interest. The red line indicates the passage southward into Davis of *RSV Aurora Australis* during Case 1, from 18 UT January 25 to 23 UT January 26, 2018. The small black filled circles indicate the locations of radiosonde launches during the three case studies. The blue contour scale indicates the mean sea ice concentration for February 2018, taken from ERA5 reanalysis.

gradients at cloud base. This method successfully identifies multiple SLW layers embedded in MPCs, which are often visible in the raw lidar data over the high-latitude Southern Ocean. The inferred cloud top height may be lower than the true cloud top due to lidar signal attenuation, but (as we will find later) the total amount of liquid water and attenuation is often small in these midlevel MPCs in the absence of precipitation.

We perform a Monte Carlo simulation using a random population of $N = 1{,}000$ samples from a normally distributed population in order to quantify the uncertainty of attributing the cloud phase (e.g., Alexander et al., 2013). For each integrated cloud attenuated backscatter β_{int} and integrated depolarization ratio δ_{int} point, we have an associated uncertainties $\Delta\beta_{int}$ and $\Delta\delta_{int}$, which we set to be twice the standard deviation of the normal distribution. We then determine the cloud phase for each of these 1,000 realizations. These simulations indicate that we misclassify around 1% of the SLW as ice across the total of 8 days of lidar observations used in these three case studies.

We also use data from the 1,290-MHz Beam-Steered Radar Wind Profiler (BSRWP) in order to characterize the horizontal wind field. These data are available at 1-h temporal resolution and at a maximum altitude of 5 km, although data gaps in the upper altitudes are not uncommon. Radiosondes were launched every 6 h from the ship for the entire summer campaign, providing a unique and valuable upper-air data set over the Southern Ocean and sea-ice zone (Sato et al., 2018). The radiosonde data are used for investigating the detailed thermodynamics during SLW and virga cases. Data from a two-channel microwave radiometer (MWR) are used to calculate liquid water path (LWP) and precipitable water vapor (PWV) (Marchand et al., 2003). ERA5 (European Centre for Medium-Range Weather Forecasting: Reanalysis Fifth Generation) (Hersbach et al., 2020) thermodynamic data at the native resolution of 0.25° × 0.25° from the nine closest grid-cells to the ship's location are interpolated to provide the vertical temperature profiles above the ship.

The primary objectives of V3 were to conduct the annual victualing resupply of Mawson station (67.6°S, 62.9°E) and retrieve summer personnel at Davis station (68.6°S, 78.0°E). We investigate three events when the ship was south of the oceanic polar front and close to East Antarctica. The area of East Antarctica relevant for this study is shown in Figure 1. The location of both stations, the ship's track into Davis and the locations of the radiosonde launches made during the three case studies are indicated. The February 2018 mean sea ice concentration from ERA5 reveals remnant sea ice present offshore from Mawson during this period. The sea conditions were calm during the sampling periods, with the small amounts of remnant first-year sea-ice acting to damp most ocean swell. We discuss details of the ship's heave, roll and pitch in the case study analyses below.

3. Results

### 3.1. Case 1: Voyage into Davis (64°S–69°S) on January 25–26, 2018

3.1.1. Overview of Event

The METOP-A satellite image of the regional cloud structure and the ERA5 500 hPa geopotential height at 04 UT January 26 is shown in Figure 2, which is a time near the start of this case study. A ridge of high pressure extends southward from the midlatitudes, with a weak short-wave trough to the west of the ship supporting extensive midlevel cloud cover above the ship's track. This large-scale midlevel cloud system propagated eastwards over the course of the January 26 and was replaced by a
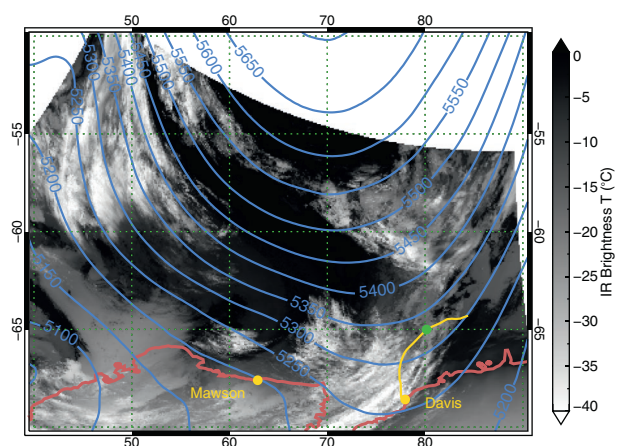
Figure 2. Infrared brightness temperature (units °C) for the METOP-A overpass at 04 UT January 26, along with the ERA5 500 hPa geopotential height at the same time (blue lines, units m). The yellow line indicates the passage southward into Davis of *RSV Aurora Australis* during Case 1, from 18 UT January 25 to 23 UT January 26, 2018, while the green filled circle indicates the ship's location at 04 UT January 26. Mawson and Davis stations are indicated by the yellow filled circles.
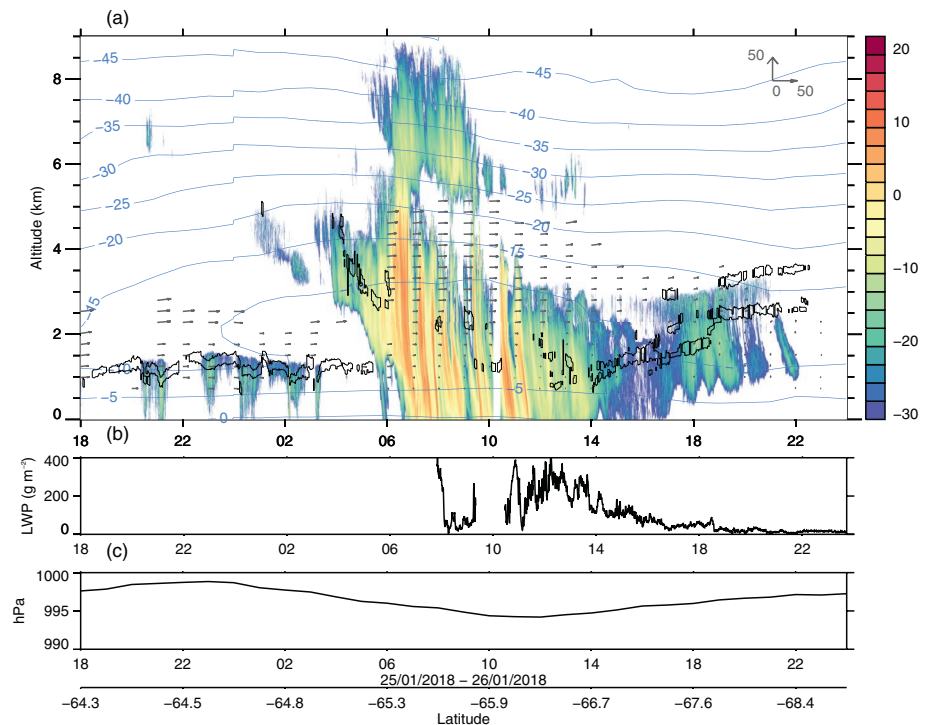
Figure 3. (a) Overview of cloud field and thermodynamic observations made during Case 1. The MWACR reflectivity is shown by the color (units dBZ). The MPL data are used to determine the location of supercooled liquid water (SLW) clouds (black outlines). The ERA5 temperature field (blue, units of °C) is indicated. A subset of the BSRWP horizontal wind field (gray vectors) is displayed for clarity. Vectors of length 50 m s^{-1} are shown in the top right of panel (a), with the upward arrow indicating the northward direction and the rightward arrow indicating eastward. (b) Liquid water path derived from the MWR: these data were unavailable for the first half of this case. (c) Surface pressure recorded onboard *RSV Aurora Australis*. The latitude of the observations is given at the bottom. MWACR, Marine W-band Cloud Radar; BSRWP, Beam-Steered Radar Wind Profiler; MWR, microwave radiometer; MPL, micropulse lidar.

homogeneous cloud layer with lower cloud tops above the ship's track (not shown). A cyclone is developing far to the west of Davis, upstream of this blocking ridge.

The cloud phase and background thermodynamic structure as observed by the MARCUS instruments on-board *RSV Aurora Australis* as the ship transited into Davis on January 25–26, 2018 are summarized in Figure 3. Solar midnight is around 19 UT at the longitude of Davis. Shallow low-level mixed-phase clouds are seen between 18 UT January 25 and 03 UT January 26 as the ship traversed latitudes 64°S–65°S. These are typical of the duration, mixed-phase, and vertical extent of boundary-layer clouds observed at lower latitudes over the Southern Ocean (Mace & Protat, 2018a; Noh et al., 2019). The hourly horizontal wind field from the BSRWP reveals a predominantly westerly flow up to the 5 km limit of wind detection. Deep precipitating ice clouds are evident between 06 UT and 14 UT January 26. Liquid layers (if present) could not be detected during these times due to attenuation of the lidar signal. Surface temperatures do not exceed freezing throughout the event. Radar reflectivities are notably lower after 14 UT January 26 and multiple SLW layers embedded within ice become evident after 16 UT January 26. Weakening southwesterly winds of <10 m s^{-1} predominate inside these trailing clouds. Attenuation of the lidar signal by low clouds means that it is only sporadically possible to detect liquid in the upper layer (between 3 and 4 km), although it seems likely that a liquid layer persists throughout. Liquid water path decreases from 12 UT January 26 onwards as the radar reflectivity drops and cloud base height rises.

3.1.2. Generating Cells

Figure 4 shows the period 17–18 UT January 26 and reveals the intricate structure of these clouds on fine temporal and spatial scales. Convective generating cells are present in the upper-level cloud region (2.3–3-km altitude) above the middle SLW layer. The MPL detects the 3 km cloud top prior to 1715 UT, before
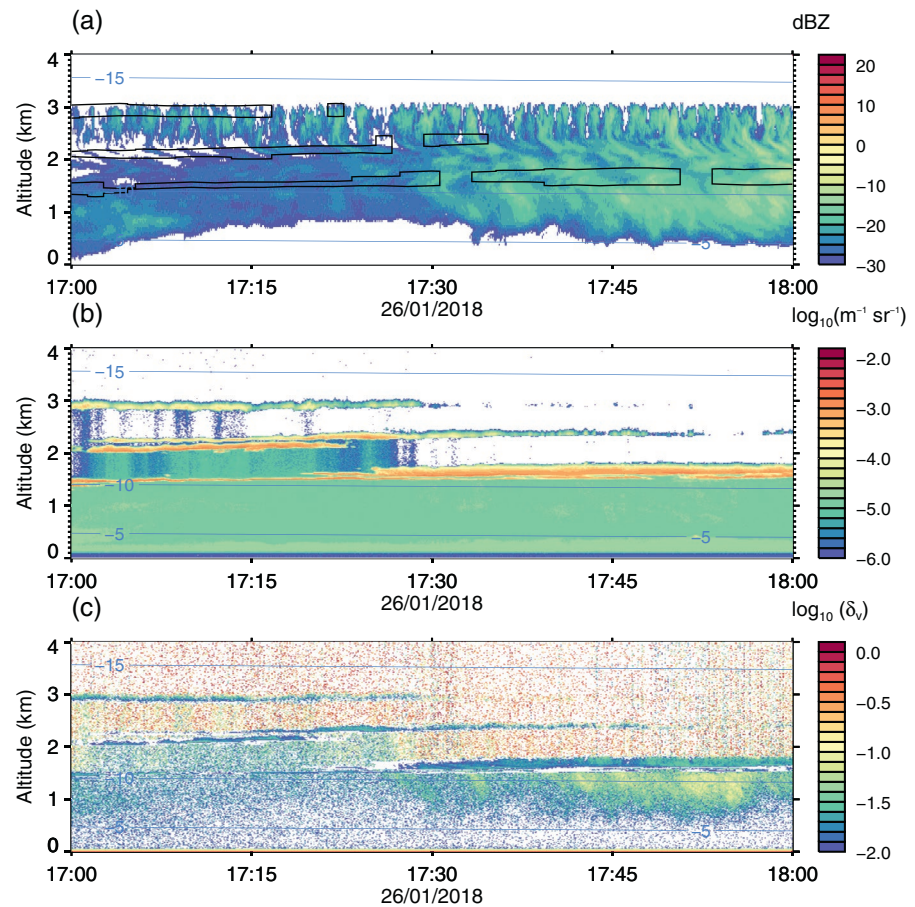
Figure 4. (a) Supercooled liquid water clouds (black outline) and MWACR reflectivity (color, units dBZ) between 17 and 18 UT January 26, 2018. (b) The MPL calibrated attenuated backscatter β_{att} and (c) the volume depolarization ratio δ_v. ERA5 temperatures (units of °C) are indicated by the blue lines on all panels. MWACR, Marine W-band Cloud Radar; MPL, micropulse lidar.

lower-level SLW layers become too optically thick. Ice is forming in the coldest, highest parts of the SLW layer, in this case at temperatures around −13°C. Ice fall streaks are readily visible in the MWACR reflectivity. Thickening of the lowest-level SLW layer inhibits identification of the SLW at upper levels after 1730 UT due to the near-full attenuation of the lidar signal. The uppermost SLW layer is present (where detectable by the MPL) inside and between GCs. This is consistent with aircraft observations which indicated minimal difference between liquid water content inside and between GCs over the open Southern Ocean (Wang et al., 2020).

The temperature, relative humidity, and wind speed and direction measured by a radiosonde launched at 1732 UT and passing through these multilayered SLW and ice virga are shown in Figure 5. A well-mixed layer, capped by a 3°C temperature inversion at SLW cloud top height, is seen in the profile of the potential temperature θ between 2.6- and 3.1-km altitude. This altitude corresponds to the convective generating cell region identified previously between the two uppermost SLW layers. Weak wind speeds of <5 m s^{-1} are present inside the cloud at altitudes below about 2.3 km, but increase to 10 m s^{-1} at cloud top. Liquid layers near 1.5 and 2 km are associated with weak temperature inversions. The θ increases inside the ice virga (above 0.5-km altitude), consistent with warming of the environment by longwave absorption by precipitating ice. The lowest-level SLW layer is capping the boundary layer (compare with Figure 4) and may be coupled with the ocean surface.

We show the MWACR reflectivity between 1719 and 1737 UT January 26 in Figure 6a, with GCs clearly visible throughout the interval. The MWACR's Doppler velocity (i.e., the sum of particle falls speed and

(a) 17:32UT 26/01/2018
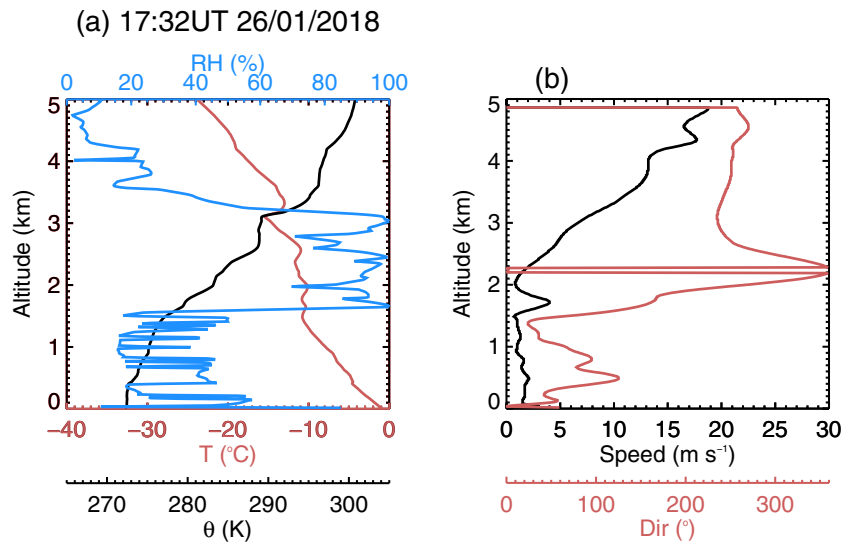
Figure 5. Radiosonde data from the 1732 UT launch on January 26, 2018. (a) Temperature (red), potential temperature (black), and relative humidity with respect to liquid (blue); (b) wind speed (black) and direction which the wind is from (red).

vertical air motion) is displayed for this interval in Figure 6b. The ship's speed over ground (seafloor) was 7 m s^{-1}, heading 175°, and the pitch and roll were always <0.2° during this time. We display the Doppler velocity profiles which have not been corrected for the ship's heave because this is negligible. Specifically, during the time interval shown in Figure 6b, the root-mean-square (rms) of the heave velocities (which were sampled at 10 Hz) was 0.07 m s^{-1}. Individual generating cells (GCs) occur in the upper part of the cloud, with a vertical extent of 0.7–0.8 km. Doppler velocities reach 1.0 m s^{-1} directly above the 2.5–2.6 km SLW layer and are close to 0 m s^{-1} at cloud top altitude of 3.1 km. The Doppler spectra are shown in Figure 6c for data collection starting at 1728 UT and lasting 2 s, which are in the middle of a convective GC. A bimodal structure is evident around 2.3-km altitude, with a secondary peak in the spectra evident at 0 m s^{-1}. This is indicative of a population of SLW droplets and corresponds to the SLW layer as visible in the MPL data. A wavelet analysis on time series of reflectivity within the GCs indicates that these predominantly had a duration of around 2 min (not shown). Given the motion of the ship at this time, and the prevailing wind speed within the clouds of 5 m s^{-1} from 240° (from Figure 5), we estimate the horizontal extent of these convective cells to be about 1.2 km.

3.1.3. SLW Layers and Precipitation Phase

Figure 7 shows the last 7 h of this event. Three separate SLW layers are identifiable between 1.5-km and 3-km altitude after 1630 UT. There is an increasing distance between the top two SLW layers, perhaps due to thermally induced circulations within the cloud driven by cloud top radiative cooling. The low volume depolarization ratio δ_v below SLW cloud base indicates that supercooled drizzle is likely falling out of these clouds prior to 17 UT. This precipitation phase transitions to be predominantly ice after 1730 UT: the δ_v below SLW cloud base increases and the LWP decreases to values close to zero which indicates insufficient liquid water for the precipitation to be drizzle. After 2030 UT, ice precipitating out of the SLW layer above 3 km sublimates before reaching the SLW layer located at 2–2.3-km altitude.

The MWACR reflectivity is larger in the ice clouds below 2 km between 1730 UT and 1930 UT than before 1730 UT, which corresponds to the time when ice falling from the highest SLW layer intercepts the second SLW layer. This increase in reflectivity can either be due to an increase in ice particle size (through riming), or an increase in ice concentration. The increased reflectivity coincides with vertically continuous observations of ice from the supercooled liquid cloud top at 3-km altitude down through all the SLW layers, i.e., seeding of the lowest boundary-layer coupled SLW cloud layer by ice produced in the generating cells at cloud top. Note that the MWACR reflectivity indicates the presence of some ice within the drizzle prior to 1730 UT.
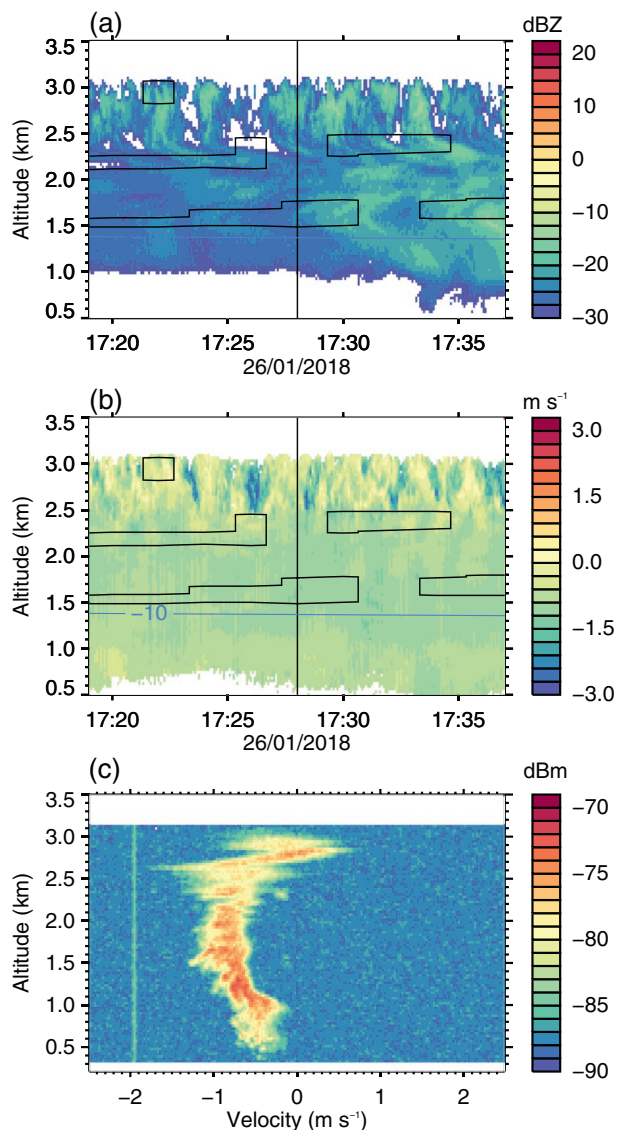
Figure 6. (a) MWACR reflectivity (dBZ) and (b) Doppler velocity (m s^{-1}, positive indicates upward motion) from 1719 to 1737 UT January 26, 2018. (c) The MWACR velocity spectra (dBm) at 1728 UT. The SLW clouds, calculated from 2-min MPL averaged data, are overlain as the black outlines in (a and b). The vertical line in (a and b) indicates the time of the spectra shown in (c). The ship's location was (67.6°S, 77.4°E) at this time. MWACR, Marine W-band Cloud Radar; MPL, micropulse lidar.

3.2. Case 2: Passage of a Cyclone Above Mawson on February 11–13, 2018

The *RSV Aurora Australis* spent nearly 2 weeks at Mawson for the annual station resupply. During "daytime" operating hours, the ship was moored in the harbor adjacent to the station. During local "night" (solar midnight is around 20 UT), or during periods of inclement weather, the ship repositioned a few nautical miles offshore. This small variation in position is insignificant for our analysis of synoptic-scale cloud systems associated with two consecutive cyclones whose centers passed north of Mawson. Broken pack-ice was still present offshore of Mawson during these 2 weeks, with a coastal polynya keeping the near-shore region largely ice-free.

3.2.1. Overview of Event

The first cyclone passage studied over Mawson occurred between February 11 and 13, 2018. Figure 8 shows the satellite image of the synoptic cloud field and 500 hPa geopotential height at 04 UT February 13, which is a time toward the end of this event. The cyclone was centered around 64°S during these 3 days and weakened as it propagated from west of Mawson station to a position north of Davis by 04 UT February 13. Earlier satellite images and ERA5 thermodynamic fields reveal a warm front preceding the cyclone's passage, while the cold front associated with this cyclone remained far to the north of the continent (not shown). The Patchy low and midlevel clouds are visible directly offshore of Mawson at 04 UT February 13 in Figure 8 in the cold sector of the cyclone, which will be discussed in detail below.

The radar reflectivity and thermodynamic profiles during the event are shown in Figure 9. Low-level wind below 1-km altitude is likely a mix of the synoptic-scale winds and an enhancement in the katabatic winds. Indeed, such wind structure observed at the East Antarctic continental margin is typically observed during the passage of offshore cyclones (Alexander et al., 2017; Orr et al., 2014). SLW layers observed by the lidar at 4–5-km altitude near the start of the event (14–16 UT February 11), along with strong westerly winds, correspond to the warm conveyor belt and the warm front as identified along coastal East Antarctica (Jullien et al., 2020). Radar reflectivity decreases and cloud top height lowers after 12 UT February 12 with evidence of multiple SLW layers within the ice clouds. MODIS Aqua retrievals (MYD06) near 10 UT on February 12 indicate the cloud top phase is liquid, with a total column optical depth between about 15 and 30 (not shown). The MARCUS MPL is heavily attenuated at this time, and is unable to detect SLW at cloud top. While it would not be surprising (given the frequent presence of SLW near cloud top), it is ambiguous as to whether or not there is liquid water at cloud top at this time or whether MODIS is responding to the liquid further down in the cloud. A single-layer MPC persists in the light wind conditions at 2-km altitude after 00 UT February 13, consistent with MODIS Terra imagery that shows thin and somewhat patchy clouds near 05 UT on February 13 (not shown; MOD06 retrievals were largely unsuccessful at this time). Note the presence of a thick ice cloud centered on 02 UT February 13 which is precipitating into the SLW. We will discuss this event in Section 3.2.3.

3.2.2. Generating Cells

Convective GCs are present during Case 2: the radar reflectivity and Doppler velocity between 1541 and 1559 UT February 15 are shown in Figure 10, along with the spectra at 1544 UT. Upward motions reaching up to 1.0 m s^{-1} are present with 0.5 km of cloud top. The temporal scale of these GCs calculated from a
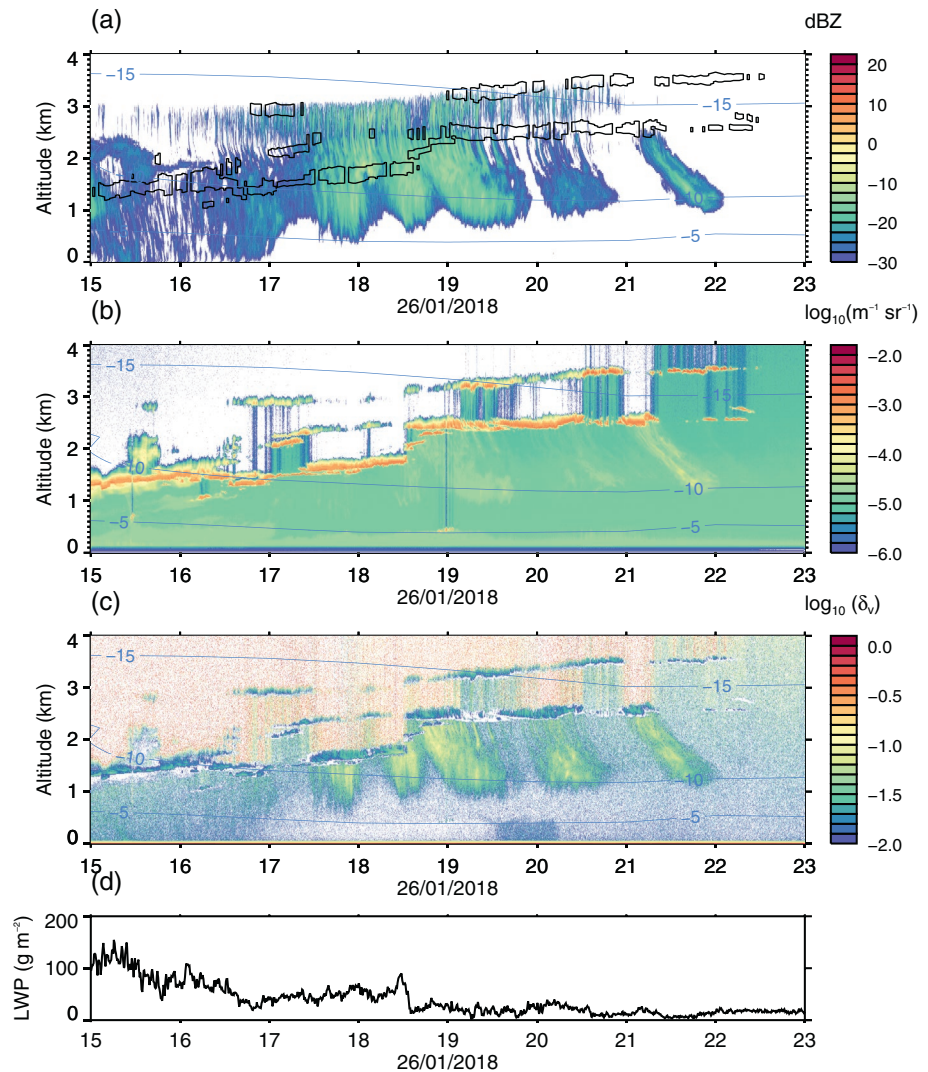
Figure 7. (a) MWACR reflectivity (color contours, units dBZ) along with the SLW cloud extent determined from the MPL data (black outlines) on January 26, 2018. (b) The MPL calibrated attenuated backscatter β_{att} during the same interval. (c) The volume depolarization ratio δ_v calculated from the MPL channels. ERA5 temperatures are indicated on all these panels (blue lines, units °C). (d) Liquid water path derived from the MWR. MWACR, Marine W-band Cloud Radar; MWR, microwave radiometer; MPL, micropulse lidar.

wavelet analysis (not shown) varies between 2 and 3 min. If we assume that the wind speed at cloud top height of these GCs is 20 m s^{-1} (the value taken from the closest radiosonde profile, launched at 1732 UT February 11), the spatial scale of these GCs is 2.4–3.6 km. The thick ice clouds fully attenuated the lidar signal (not shown) thus we have no information on the presence or absence of SLW within these GCs, but microwave radiometer data indicate that liquid water is present during this time.
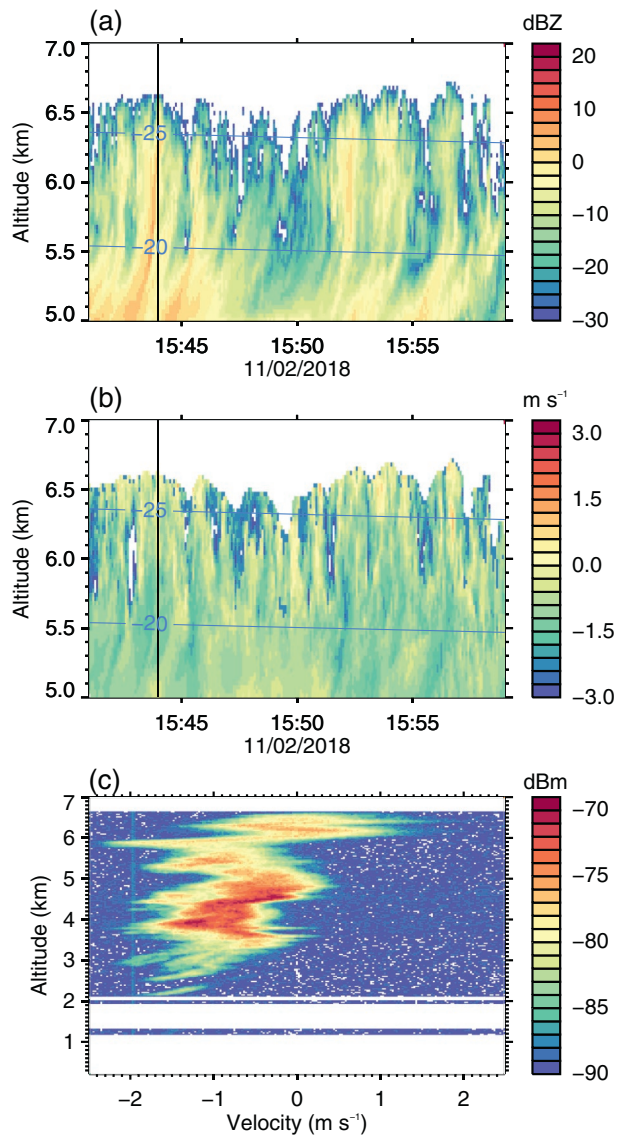
3.2.3. SLW Layers and Precipitation Phase

Figure 11 shows details of the clouds observed toward the end of the Case 2 cyclone. Similar to the observations made of Case 1 (the transit into Davis), multiple layers of SLW clouds are apparent, although it is difficult to identify the SLW layer at ice cloud top before 18 UT February 12 due to opaque lower-level SLW layers. The SLW layer around 3-km altitude ascends in time and corresponds to a narrow vertical band with a decrease in MWACR reflectivity (most clearly visible in Figure 11a directly after the 1800 UT SLW layer, or directly before the 1930 UT SLW layer).
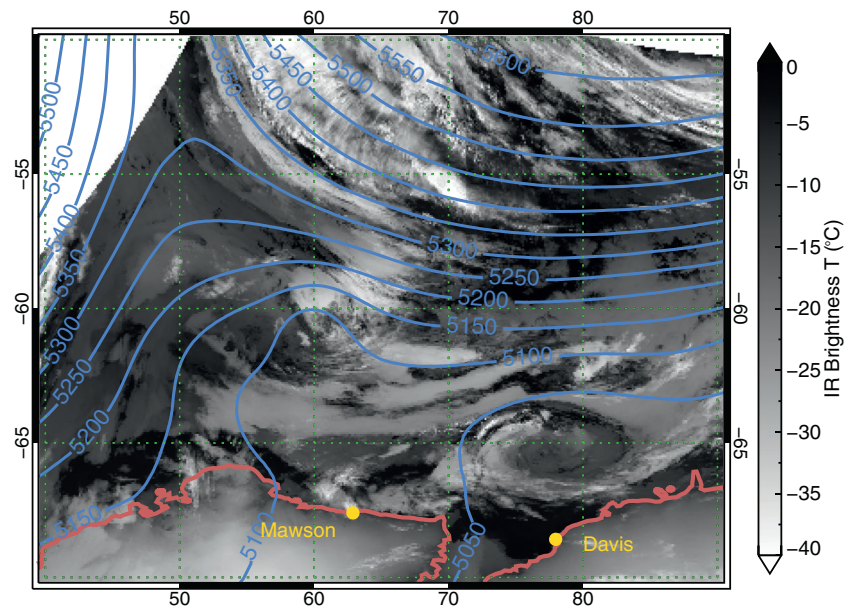
Figure 8. Infrared brightness temperature (units °C) for the METOP-B overpass at 04 UT February 13, along with the ERA5 500 hPa geopotential height at the same time (blue lines, units m). The ship is at Mawson station.
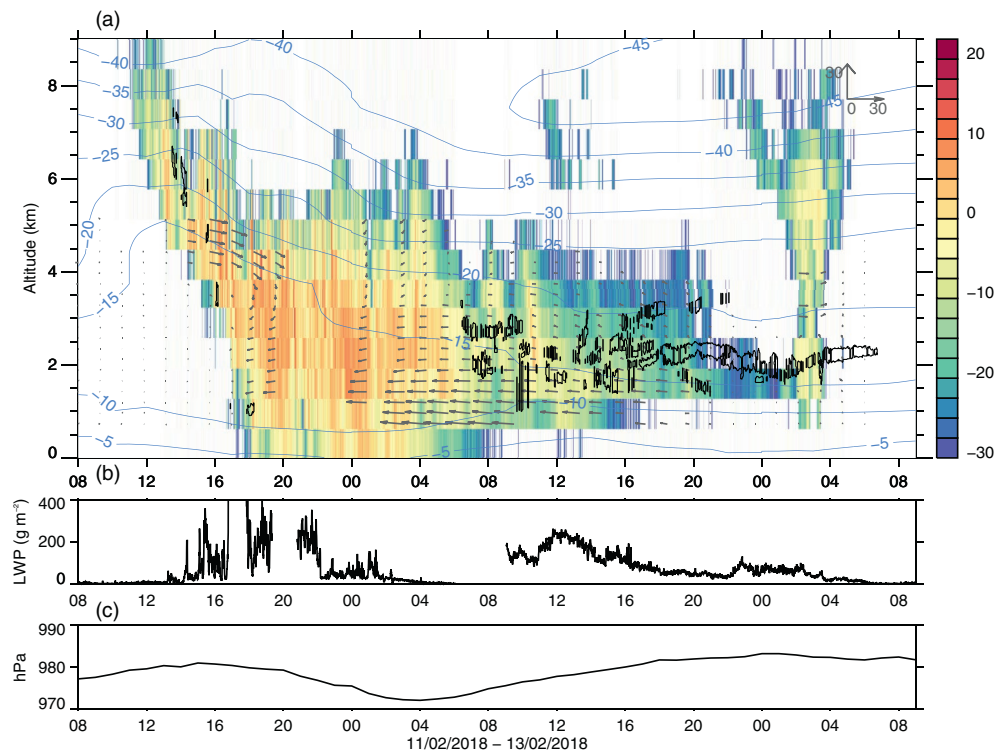
Figure 9. As for Figure 3 except showing the cloud and thermodynamic fields during Case 2, February 11–13, 2018, when the ship was at Mawson. Vectors of length 30 m s^{-1} are shown in the top right of panel (a), with the upward arrow indicating the northward direction and the rightward arrow indicating eastward. Data gaps in the MWR LWP and the BSRWP winds are evident. MWR, microwave radiometer; LWP, liquid water path; BSRWP, Beam-Steered Radar Wind Profiler.

Figure 10. (a) MWACR reflectivity (dBZ) and (b) Doppler velocity (m s⁻¹, positive indicates upward motion) from 1541 to 1559 UT February 11, 2018. (c) The MWACR velocity spectra (dBm) at 1544 UT (note the different *y* axis in this panel, from surface to cloud top). The vertical line in (a and b) indicates the time of the spectra shown in (c). MWACR, Marine W-band Cloud Radar.

A layer of SLW with base around 2 km is identified throughout this part of the event. The δ_v beneath this SLW layer (Figure 11c) indicate the presence of supercooled drizzle between 00 and 02 UT February 13. The sudden increase in δ_v below the SLW layer after 02 UT February 13 indicates the dominance of precipitating ice, although we cannot rule out the possibility of small amounts of supercooled drizzle also being present. The liquid water path (Figure 11d) is large enough to support the existence of supercooled drizzle during this time. The observation of precipitating ice between 0200 and 0330 UT matches the intersection of the 2-km altitude SLW layer by a high-level ice cloud (Figure 11a).

The two radiosonde profiles obtained during this interval (Figure 12) indicate an inversion layer at cloud top height (an inversion of 3°C at 4 km at 1730 UT; and 4°C at 2.5 km at 2332 UT). The θ profile below cloud top indicates a well-mixed region inside the MPC at 2332 UT. A shallow, well-mixed near surface layer due to the katabatic wind is apparent at 2332 UT. The strong wind shear above the jet may be an intense source of mixing.
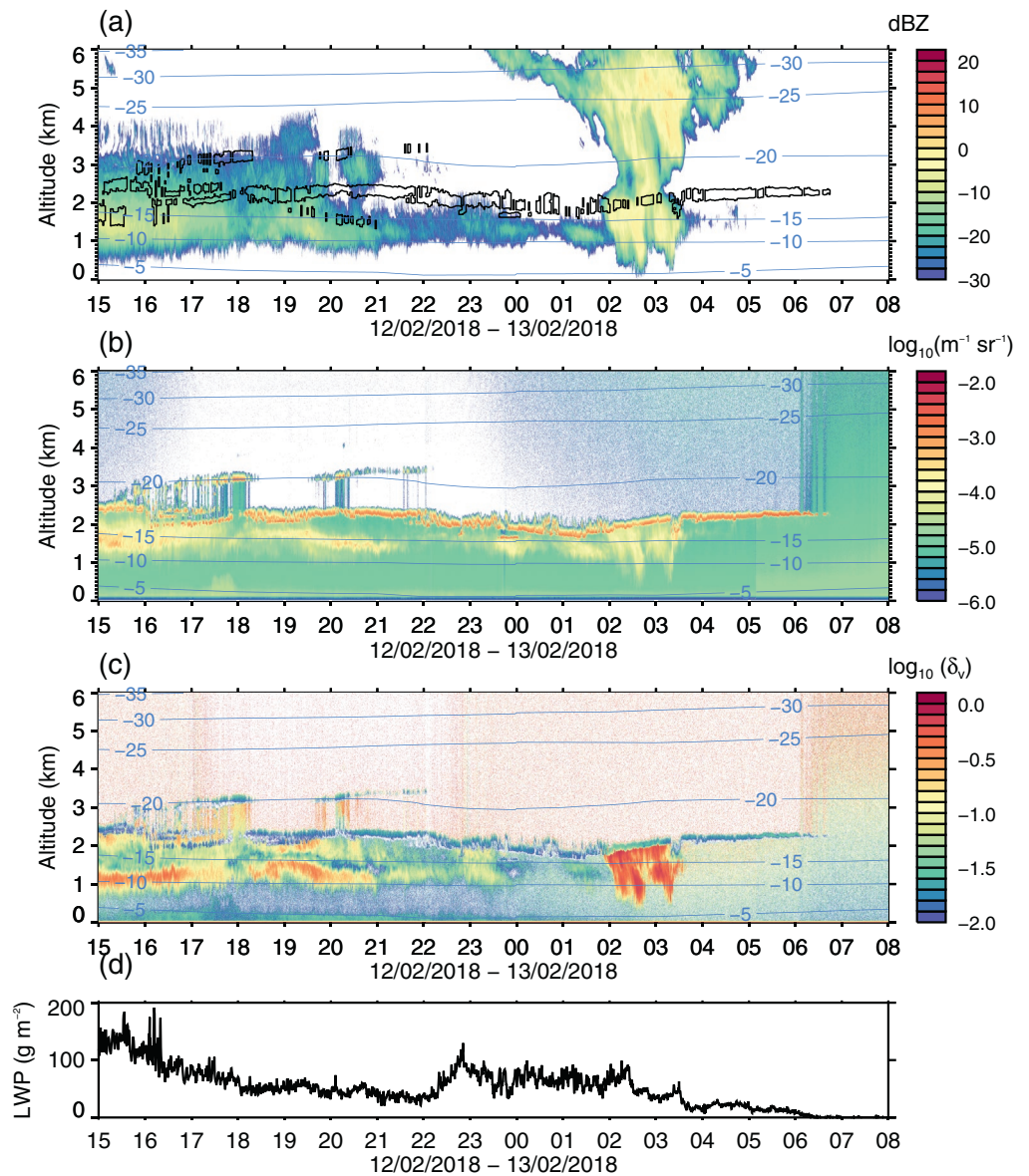
3.3. Case 3: Passage of the Following Cyclone Above Mawson on February 14–16, 2018

3.3.1. Overview of Event

The following cyclone also passed north of Mawson and produced cloud bands visible above the ship from February 14 to 16, 2018. Midlevel ice seeding and a single SLW layer precipitating ice at temperatures below −30°C will be described, but for this case we find no evidence of supercooled drizzle, which is in contrast to the two prior case studies. The imminent arrival at Mawson of the cyclone's warm front and associated cloud bands are visible in the satellite cloud image and geopotential height data at 19 UT February 14 in Figure 13. The cold front associated with this cyclone, as with the previous Mawson cyclone, remained well to the north of the continent (not shown, see Vignon et al. [2021] for further details). Satellite images and thermodynamic data from later times indicate that this cyclone weakened as it propagated south-eastward toward the coast, with cloud dissipating in a midlevel westerly flow on January 16 (not shown).

Boundary-layer mixed-phase clouds are present before 20 UT February 14, preceding the arrival of the warm front. A mixed-phase cloud (liquid water layer at 5.7 km precipitating ice virga) is present from 16 UT February 14 (Figure 14). These high-level SLW clouds are commonly observed over the Southern Ocean (McFarquhar et al., 2021). This mixed-phase cloud descends in time, maintaining cloud top temperatures of about −30°C. Liquid water path (LWP) is much larger when shallow boundary-layer mixed-phase clouds are observed than when only the midlevel SLW layer is present. The horizontal wind field within the ice remains light (at least at altitudes below 5 km, which is the maximum range of the BSRWP). Similar to the previous case study, winds above 4-km altitude veer from northwesterly to northeasterly and the temperature rises above 3-km altitude as the cloud base height decreases. The winds and SLW clouds again indicate the presence of a warm front, following the model of Keppas et al. (2018). Thick ice clouds persist until around 06 UT February 16, well after the surface pressure starts to rise. Single layers of SLW cloud occur in regions of light wind from about 11 UT February 16 onward.
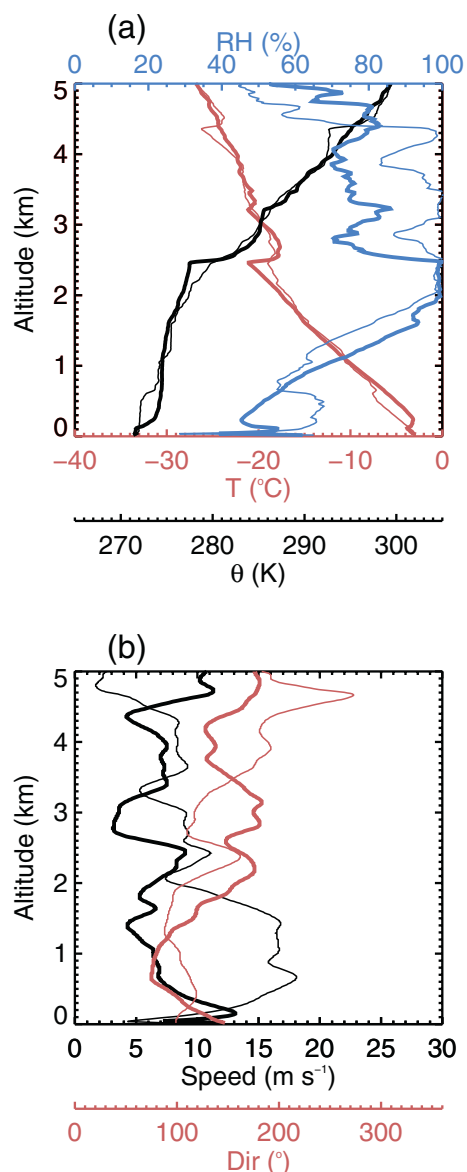
Figure 11. As for Figure 7, except showing the observations between 15 UT February 12 and 08 UT February 13, 2018.

3.3.2. Generating Cells

The radar reflectivity, Doppler velocity, and spectra of the GCs present between 1039 and 1057 UT February 15 are shown in Figure 15. The thick ice clouds fully attenuated the lidar signal (not shown) thus we have no information on the presence or absence of SLW within these GCs, but microwave radiometer data indicate the presence of liquid water. The Doppler velocities are displayed without correction for the negligible heave velocities during this time interval: the rms heave velocity during this time was 0.004 m s^{-1}. The overall features of the GCs seen in this event are consistent with those reported in Case 1 and Case 2. GCs have vertical extent around 0.9 km, fall streaks are clearly evident, and the wavelet spectra indicate dominant temporal scales of 1 and 3 min (not shown). Wind speeds at cloud top height were around 10 m s^{-1} (obtained from the 1130 UT radiosonde profile, not shown), thus the spatial scale of these GCs varied from 0.6 to 1.8 km during this interval. The Doppler velocity spectra at 1048 UT, in the middle of a GC, indicate velocities around 0 m s^{-1} between cloud top and about 4.1-km altitude, with the falling (negative velocities)

Figure 12. Radiosonde data from the 1730 UT (thin) and 2332 UT (thick) launches on February 12, 2018. (a) Temperature (red), potential temperature (black), and relative humidity with respect to liquid (blue); (b) wind speed (black) and direction which the wind is from (red).

particles clearly evident at lower altitudes. The bimodality around 3.8-km altitude (at the base of the GCs) suggests the presence of a second SLW droplet population.
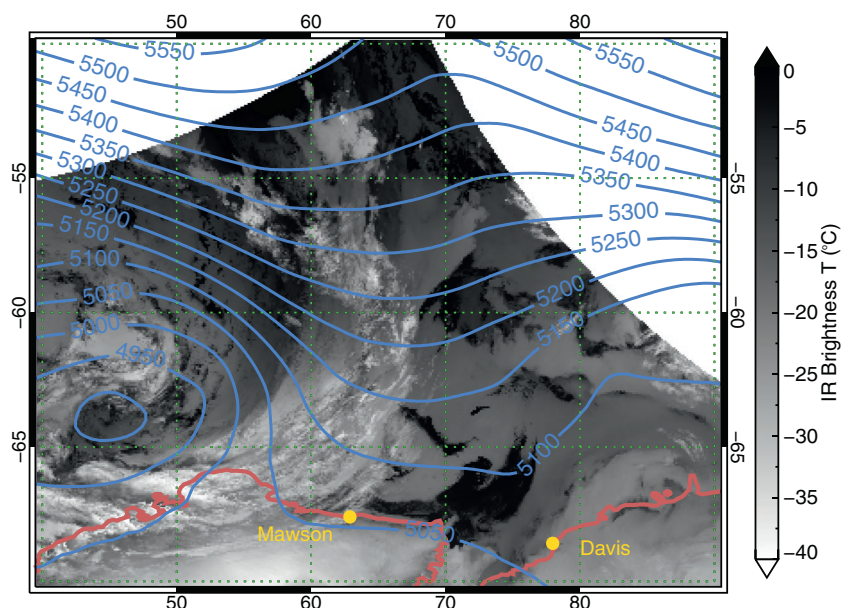
3.3.3. SLW Layers and Precipitation Phase

Figure 16 shows the clouds and precipitation observed toward the end of the passage of the Case 3 cyclone. Although thick, low-level SLW cloud identified in the MPL data before 10 UT mostly obscures the clouds at higher levels, we can see that SLW clouds exist above 4 km at temperatures as low as −31 °C. There are two distinct high-altitude SLW cloud layers just above, at 07 UT, separated vertically by about 500 m. The highest SLW layer does not appear to be precipitating. Likewise, a careful examination of the low-level SLW clouds suggests that there are two SLW layers here.

After 11 UT, a precipitating SLW cloud layer persists for 2 h at an altitude of 4.2 km and cloud top temperature of −31°C. Retrievals from MODIS Aqua taken near 11 UT and MODIS Terra near 0530 UT on February 16 (MYD/MODIS products) both indicate the region near the ship covered by primarily liquid phase clouds with a cloud top near 4 km, along with some smaller patches of ice cloud (not shown). Liquid particle effective radius was near or below 10 μm, with lower overall optical depths during the overpass near 11 UT, all of which is consistent with the radar and lidar observations. The δ_v (Figure 16c) indicates the predominance of ice precipitation beneath this midlevel cloud. Streaks of ice from higher altitudes (visible in the MWACR data in Figure 16a) intercept this SLW layer on occasion, which act to seed the SLW layer. These seeding events may be a factor in the decay of the SLW layer. The radiosonde launched at 1130 UT (Figure 17) passed through this virga and SLW layer: the stable top above the SLW layer around 4.5-km altitude is clearly evident. The thermodynamic profiles below 0.5-km altitude again show the typical characteristics of the katabatic wind at Mawson (Vignon et al., 2019). The well-mixed convective boundary layer tops out around 1.7 km, which corresponds to cloud virga base. The liquid water path (LWP) is low during this event and there is little, if any, evidence for supercooled drizzle.

4. Discussion

The synoptic structure differed for each of the three cases examined here, yet all revealed the prevalence of MPCs. Extensive clouds observed during the transit into Davis existed due to the presence of a weak trough, whereas observations made during the two Mawson-based case studies encompassed both the warm and cold sectors of the cyclones. For the two Mawson case studies, the cyclones decayed as they propagated eastward.

All events showed the typical three stages of cloud and precipitation observed in cloud systems along the East Antarctic coastline, specifically, (i) preprecipitation virga falling out of SLW layers at the start of the event, (ii) precipitation reaching the surface (characterized by the strong radar reflectivities) during the event, and finally (iii) postprecipitation virga in the trailing SLW layers (Jullien et al., 2020), Multiple layers of SLW cloud were embedded within ice clouds of large vertical extent (i.e., several kilometers deep) for several hours during the central phase of each event (see Figures 3, 9, and 14). This consistent cloud and virga/precipitation structure observed during all three events suggests the ubiquitous occurrence of SLW layers within synoptic-scale cloud systems in the high-latitude austral summer Southern Ocean.

However, small differences in precipitation phase, cloud seeding, and the altitude of the trailing clouds were observed between events. The trailing clouds observed during the events consisted of a single SLW layer

Figure 13. Infrared brightness temperature (units °C) for the METOP-B overpass at 19 UT February 14, along with the ERA5 500 hPa geopotential height at the same time (blue lines, units m). The ship is at Mawson station.
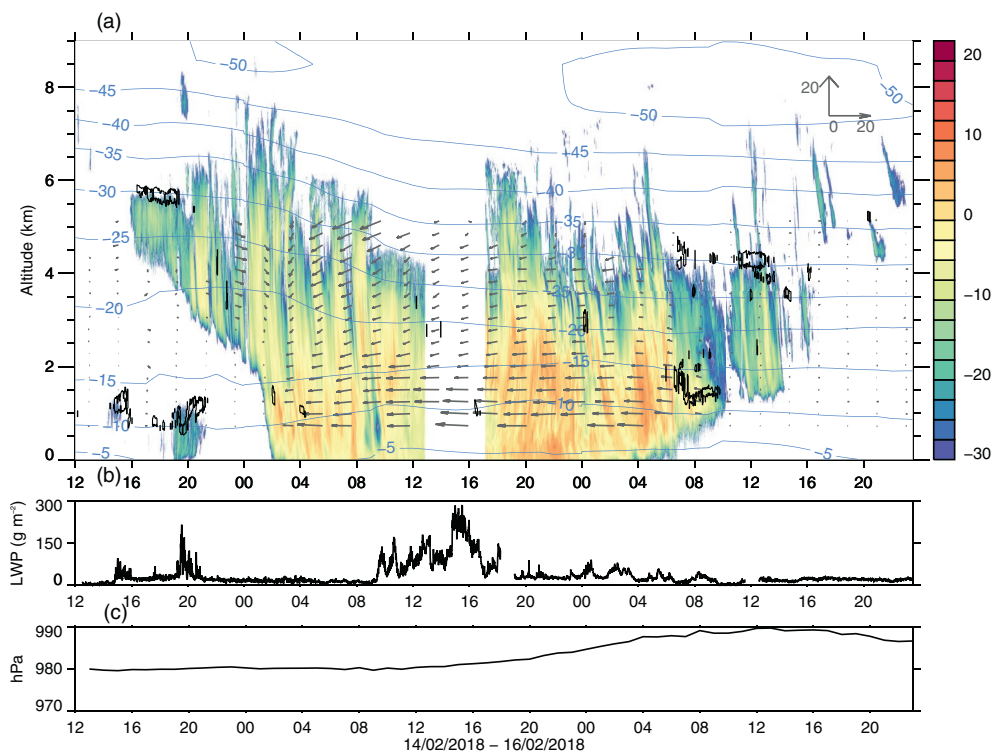
Figure 14. As for Figure 3 except showing the cloud and thermodynamic fields during Case 3, February 14–16, 2018, when the ship was at Mawson. Vectors of length 20 m s^{-1} are shown in the top right of panel (a), with the upward arrow indicating the northward direction and the rightward arrow indicating eastward. The MWACR cloud radar was not operational between 13 and 17 UT, February 15. MWACR, Marine W-band Cloud Radar.
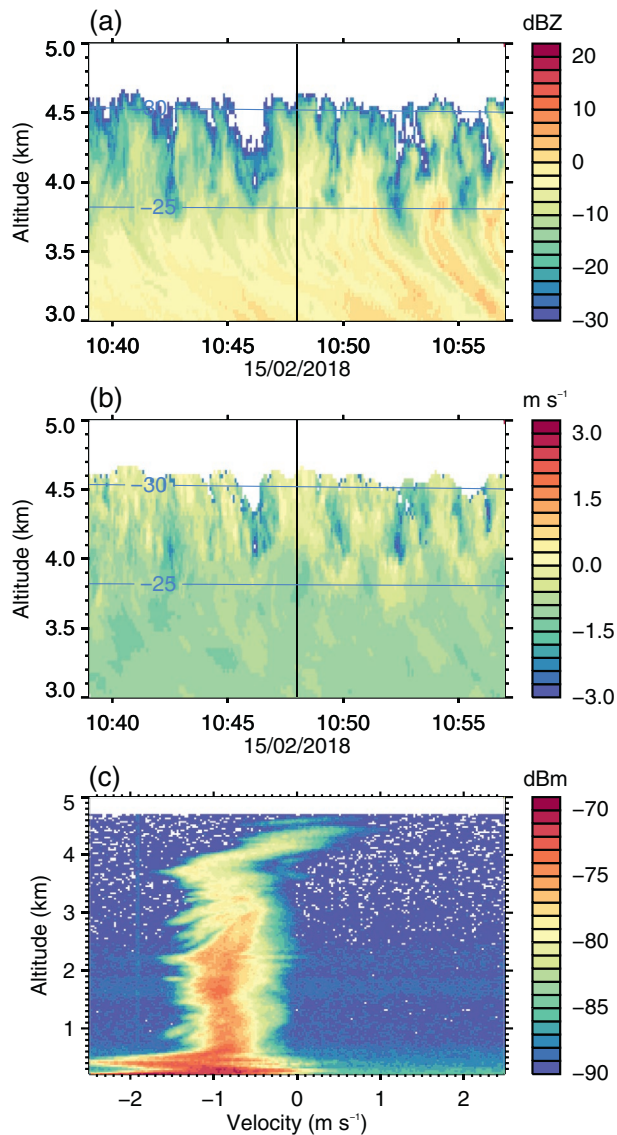
Figure 15. (a) MWACR reflectivity (dBZ) and (b) Doppler velocity (m s^{-1}, positive indicates upward motion) from 1039 to 1057 UT February 15, 2018. (c) The MWACR velocity spectra (dBm) at 1048 UT (note the different y axis in this panel, from surface to cloud top). The vertical line in (a and b) indicates the time of the spectra shown in (c). MWACR, Marine W-band Cloud Radar.

in regions of very light wind speeds (<5 m s^{-1}) either at the top of the boundary layer (Case 2) or as part of a midlevel MPC (Case 1 and Case 3). SLW cloud top temperatures during Case 3 were no warmer than −31 °C. In all three cases, ice precipitation from the single SLW layer continues for several hours. Ice precipitation was enhanced during Case 2 and Case 3 at Mawson by higher-level seeder ice clouds feeding the SLW layer (Figures 11 and 16), similar to cloud seeding of midlevel SLW layers reported in the tropics (Ansmann et al., 2009), northern midlatitudes (Herzegh & Hobbs, 1980; Hobbs et al., 1980), and the Arctic (Hobbs & Rangno, 1998).

Generating cells and their associated precipitating ice fall streaks have been extensively documented for extratropical Northern Hemisphere cyclones; recent examples include Kumjian et al. (2014), Rosenow et al. (2014), Rauber et al. (2015), and Keppas et al. (2018). We summarize our findings for the generating cells observed adjacent to the Antarctic in Table 2. GCs with similar physical characteristics to these Antarctic cases were recently observed over the continental United States (Evans et al., 2005; Rosenow et al., 2014) and the Arctic (McFarquhar et al., 2011). The mean horizontal extent of GCs reported from aircraft observations over the open Southern Ocean is 0.4 km (Wang et al., 2020), lower than the cases adjacent to East Antarctica discussed here. This difference may be due to either a different environment close to the Antarctic (subject to maritime and continental influences), or the limited number of samples discussed here. Our observations of a large range in temperatures of the GCs (−13°C to −30°C) is consistent with the spread noted elsewhere (Evans et al., 2005; Kumjian et al., 2014).

The GCs reported directly offshore of Antarctica exist in midlevel clouds which are topped by an SLW layer (which is either seen directly by the lidar, or inferred based on large vertical motion and temperature inversion reported by radiosonde), and all exhibited ice precipitation. Air-motion induced oscillations are evident in the GC regions near cloud tops. A region of increasing negative (downward) Doppler velocity is present beneath the GC turbulence region which is likely due to the growth of solid particles in the more quiescent air. This particle growth could be due to riming, which increases the mass to cross-sectional area ratio. Doppler velocities are maximum downward above 1.5 km (the altitude of the lowest SLW layer) for the January 26 event offshore of Davis (Figure 6). The ice particles then sublimate in the very dry air below this lowest SLW layer and Doppler velocities increase near the base of the cloud. This increase is likely due to snow losing cross-sectional area and becoming more spherical as the particles become smaller, thereby increasing velocity even as the total condensed mass decreases. The widths of the Doppler spectra near cloud base (or surface) are much larger for the two Mawson cases than the first case. The narrowness of the January 26 event suggests a nearly mono-dispersive snow power spectral density (assuming little to no turbulence or mean motion in the subcloud region), while the two Mawson cases have much broader spectra. In particular, the Doppler spectra for 1048 UT February 15 is very broad below 0.5-km altitude (Figure 15c). The radiosonde profile from 1130 UT February 15 clearly indicates a well-mixed katabatic layer at these low altitudes which is sufficiently turbulent to alter the Doppler motion of the precipitating ice.

Observations of the multiple SLW layers during Case 1 (Figure 7) and coincident radiosonde profile data indicate that the lowest SLW cloud layer is likely associated with the convective boundary layer while the top SLW layer is likely due to turbulent updrafts. Turbulence driven by cloud top radiative cooling of the upper SLW layer, in which generating cells are evident (see Figure 6), is likely the main driver of the updrafts
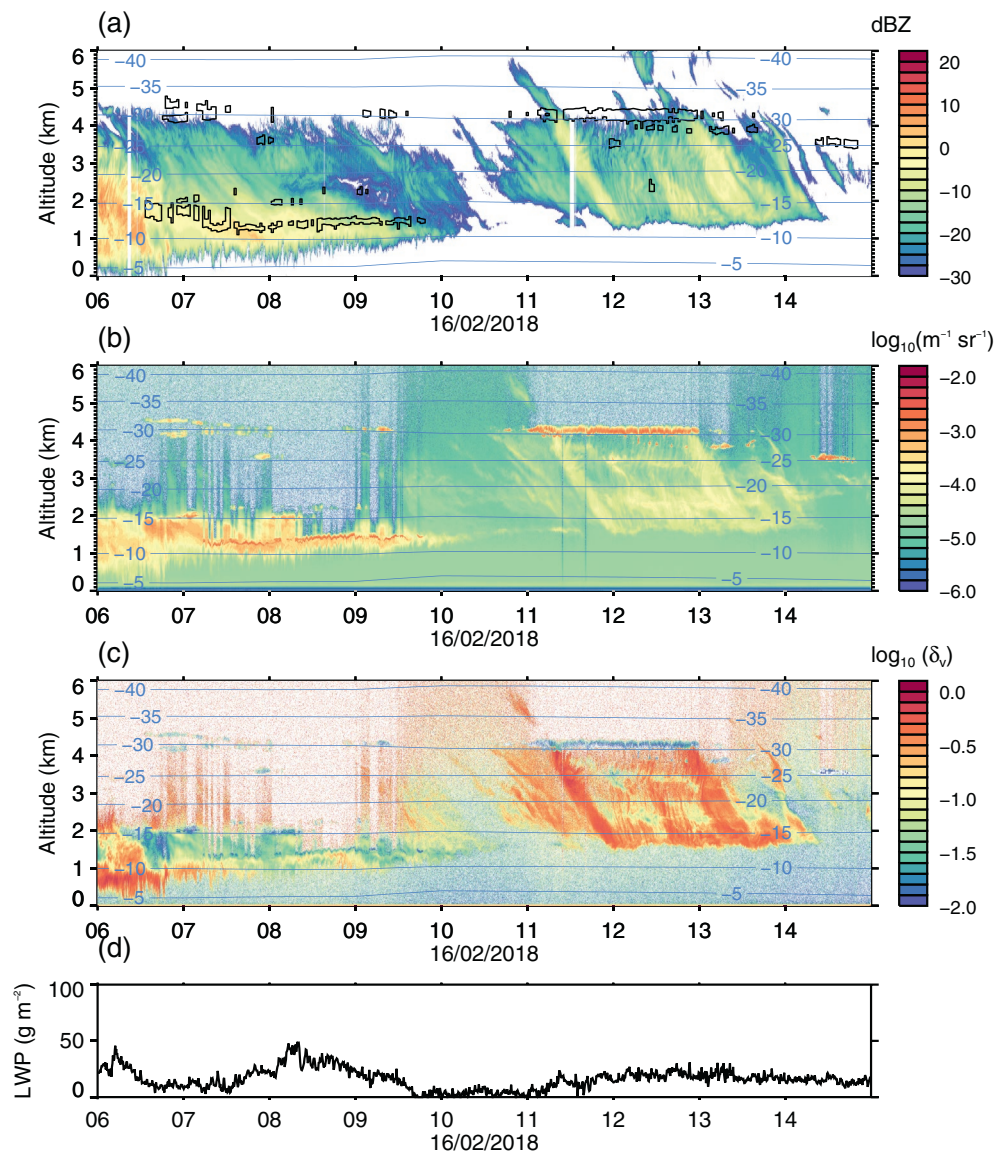
Figure 16. As for Figure 7, except showing the observations between 06 UT and 15 UT February 16, 2018.

(Heymsfield et al., 1991; Hogan et al., 2003), although the strong wind shear within the cloud will also enhance mixing in this layer. In Case 1, a third (middle) SLW layer around 2.3 km is apparent before 19 UT. All three cases featured such embedded (multiple) SLW layers, consistent with the idea that embedded SLW layers within deep ice clouds can be driven by turbulent mixing, and will persist as long as turbulent processes continue (Field et al., 2014). Multiple SLW layers can additionally be maintained via the longwave radiative effect. Cloud-resolving modeling of Arctic multilayer MPCs indicated that cloud base radiative warming of the upper layer creates a gap in stability between two MPC layers (Luo et al., 2008).

Precipitation out of the base of the SLW layers changed phase in two of the three case studies, in both cases near the end of the event. The supercooled drizzle persisted for about 2 h in both cases, before changing to predominantly ice precipitation. The LWP during both precipitating drizzle episodes is 50–100 g m^{-2}. Nonprecipitating SLW clouds in the midlatitude Southern Ocean generally have LWP <50 g m^{-2} (Mace & Protat, 2018b). The LWP in the present high-latitude Southern Ocean studies are large enough that drizzle is likely present during the periods identified in Section 3, while supercooled drizzle is either light or not likely present once the LWP dropped well below 50 g m^{-2}. The phase change from supercooled drizzle to
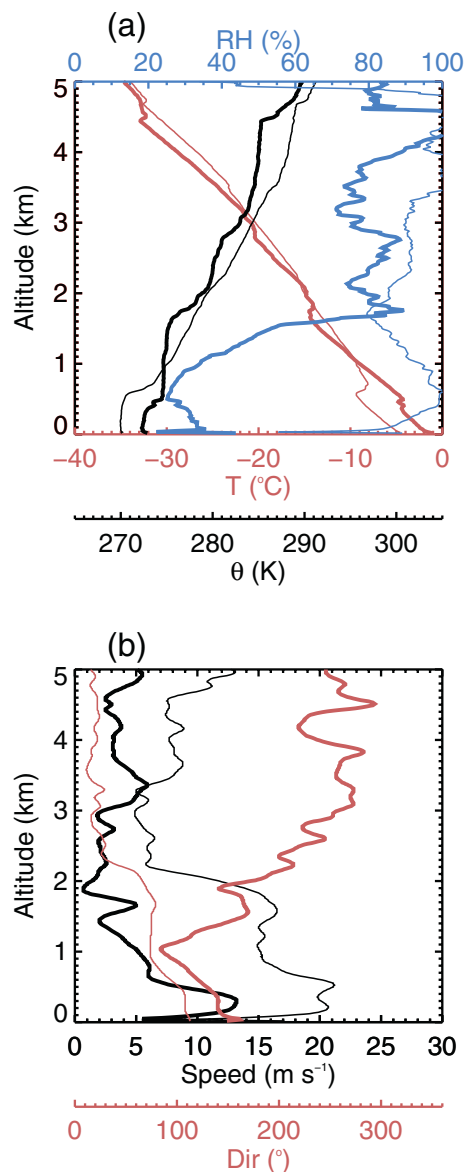
Figure 17. Radiosonde data from the 1130 UT February 15 (thin) and 1130 UT February 16 (thick) launches. (a) Temperature (red), potential temperature (black), and relative humidity with respect to liquid (blue); (b) wind speed (black) and direction which the wind is from (red).

ice precipitation was associated with seeding from higher clouds. Supercooled drizzle was present at temperatures between $-15°C$ (cloud base) and $-2°C$ (close to the surface) during these two events. Secondary ice multiplication processes will lead to an increase in ice crystal number concentration within these temperature ranges (Hallett & Mossop, 1974). Given the presence of supercooled drizzle in two out of the three cases presented here, it is likely that this is a common occurrence in cyclonic systems above the Southern Ocean and coastal Antarctic, including within the Hallett-Mossop zone. Supercooled drizzle-sized droplets potentially have important implications for secondary ice production processes over the high-latitude Southern Ocean (Young et al., 2018) as the freezing drizzle is suspected to eject many small droplets, favoring ice multiplication (Korolev et al., 2020).

5. Conclusions

Cloud remote-sensing instruments including W-band radar, a micropulse lidar and a microwave radiometer were mounted aboard an icebreaking vessel *RSV Aurora Australis* during austral summer 2017–2018 as it transited the Southern Ocean. We characterize the fine-scale vertical structure and evolution of clouds and precipitation phase present in three systems which passed over the ship when it was between 64°S and 69°S, close or adjacent to the East Antarctic coast.

Multiple layers of SLW were embedded within ice clouds (with cloud tops of 2–6-km altitude). The trailing clouds observed in these systems were SLW-topped MPCs, which continued to precipitate ice, either at the top of the boundary layer or at midlevels. This ice precipitation out of the SLW was enhanced in some cases by seeding from higher-level ice clouds. Ice precipitation is nearly continuous in all but the trailing SLW cloud layer(s) observed as the cyclonic systems are advected away from the ship.

Convective generating cells (GCs) were present within midlevel SLW layer topped MPCs and had physical scales (vertical extents up to 1.0 km and horizontal extent up to 3.6 km) and upward Doppler motions (0.5–1.0 m s^{-1}) consistent with observations of GCs made previously at lower latitudes. Supercooled drizzle was observed during two of the three events studied. In both cases the precipitation phase changed from drizzle to predominantly ice following seeding of the drizzling SLW layer by a higher-level ice cloud. The supercooled drizzle events both persisted for around 2 h, and the drizzle was present in temperatures as cold as $-15°C$ and as warm as $-2°C$.

Following this characterization of the fine-scale structure of mixed-phase clouds and precipitation within cyclones adjacent to the Antarctic, the next step is to simulate these events in high-resolution models. Although it is likely that models will have difficulty producing and maintaining SLW, we suspect that by appropriately tuning the microphysical schemes using MARCUS observations, we will be able to more accurately reproduce the clouds' vertical structure, evolution, and phase partitioning (Vignon et al., 2021). Such a path to model improvement of Southern Ocean clouds could be informed by recent analyses of geostationary satellite imagery, which are capable of providing cloud macrophysical properties and information on subcloud phase beneath supercooled liquid cloud tops (e.g., Noh et al., 2019).

Table 2
Physical Characteristics of Generating Cells Observed Adjacent to Antarctica

Case	Date	T (°C)	Horizontal extent (km)	Vertical extent (km)	Maximum upward Doppler velocity (m s^{-1})
1	January 26	−13	1.2	0.7–0.8	1.0
2	February 11	−26	2.4–3.6	1.0	1.0
3	February 15	−30	0.6–1.8	0.9	0.5

The temperature T, From ERA5, given below is that at cloud top height. Horizontal extent of the GCs are calculated using the radiosonde-derived wind speeds and directions, and the ship motion, as described in Section 3. The Doppler velocities given here are not corrected for the ship's negligible heave velocities (see text for details).

Data Availability Statement

MARCUS data were obtained from the Atmospheric Radiation Measurement (ARM) Program sponsored by the U.S. Department of Energy, Office of Science, Office of Biological and Environmental Research, and Climate and Environmental Sciences Division. We thank all of the ARM technicians who collected the data and maintained the instruments onboard *RSV Aurora Australis*. ARM-MARCUS data used in this study may be downloaded from https://adc.arm.gov/discovery/, while ERA5 data are available at https://cds.climate.copernicus.eu/. METOP satellite images are available at https://navigator.eumetsat.int/ Ship surface meteorological and position data are available through the Australian Antarctic Data Centre https://data.aad.gov.au. The MPL calibrated backscatter and derived cloud phase products, along with the LWP and IWC from the MWR are permanently archived at https://data.aad.gov.au/metadata/records/AAS_4292_MARCUS_Case_Studies (Alexander, 2020). All data are freely available following registration.

References

Alexander, S. P. (2020). *Derived data products produced from MARCUS cyclone observations, January-February, 2018*. Australian Antarctic Data Centre. https://doi.org/10.4225/15/58eedd2fd5a6b

Alexander, S. P., Klekociuk, A. R., McDonald, A. J., & Pitts, M. C. (2013). Quantifying the role of orographic gravity waves on polar stratospheric cloud occurrence in the Antarctic and the Arctic. *Journal of Geophysical Research: Atmospheres*, 118, 11493–11507. https://doi.org/10.1002/2013JD020122

Alexander, S. P., Orr, A., Webster, S., & Murphy, D. J. (2017). Observations and fine-scale model simulations of gravity waves over Davis, East Antarctica (69°S, 78°E). *Journal of Geophysical Research: Atmospheres*, 122, 7355–7370. https://doi.org/10.1002/2017JD026615

Alexander, S. P., & Protat, A. (2018). Cloud properties observed from the surface and by satellite at the northern edge of the Southern Ocean. *Journal of Geophysical Research: Atmospheres*, 123, 443–456. https://doi.org/10.1002/2017JD026552

Alexander, S. P., & Protat, A. (2019). Vertical profiling of aerosols with a combined Raman-elastic backscatter lidar in the remote Southern Ocean marine boundary layer (43°S-66°S, 132°E-150°E). *Journal of Geophysical Research: Atmospheres*, 124, 12107–12125. https://doi.org/10.1029/2019JD030628

Ansmann, A., Tesche, M., Seifert, P., Althausen, D., Engelmann, R., Fruntke, J., et al. (2009). Evolution of the ice phase in tropical altocumulus: SAMUM lidar observations over Cape Verde. *Journal of Geophysical Research*, 114, D17208. https://doi.org/10.1029/2008JD011659

Barrett, P. A., Blyth, A., Brown, P. R. A., & Abel, S. J. (2020). The structure of turbulence and mixed-phase cloud microphysics in a highly supercooled altocumulus cloud. *Atmospheric Chemistry and Physics*, 20, 1921–1939. https://doi.org/10.5194/acp-20-1921-2020

Burrows, S. M., Hoose, C., Pöschl, U., & Lawrence, M. G. (2013). Ice nuclei in marine air: Biogenic particles or dust? *Atmospheric Chemistry and Physics*, 13, 245–267. https://doi.org/10.5194/acp-13-245-2013

Ceppi, P., Hartmann, D., & Webb, M. J. (2016). Mechanisms of the negative shortwave cloud feedback in middle to high latitudes. *Journal of Climate*, 29, 139–157. https://doi.org/10.1175/JCLI-D-15-0327.1

Choi, Y. S., Ho, C. H., Park, C. E., Storelvmo, T., & Tan, I. (2014). Influence of cloud phase composition on climate feedbacks. *Journal of Geophysical Research: Atmospheres*, 119, 3687–3700. https://doi.org/10.1002/2013JD020582

Chubb, T. H., Jensen, J. B., Siems, S. T., & Manton, M. J. (2013). In situ observations of supercooled liquid clouds over the Southern Ocean during the HIAPER Pole-to-Pole Observation (HIPPO) campaigns. *Geophysical Research Letters*, 40, 5280–5285. https://doi.org/10.1002/grl.50986

Cunningham, J. G., & Yuter, S. E. (2014). Instability characteristics of radar-derived mesoscale organization modes within cool-season precipitation near Portland, Oregon. *Monthly Weather Review*, 142, 1738–1757. https://doi.org/10.1175/MWR-D-13-00133.1

Evans, A. G., Locatelli, J. D., Stoelinga, M. T., & Hobbs, P. V. (2005). The IMPROVE-1 storm of 12 February 2001. Part II: Cloud structures and the growth of precipitation. *Journal of the Atmospheric Sciences*, 62, 3456–3473. https://doi.org/10.1175/JAS3547.1

Field, P. R., Hill, A. A., Furtado, K., & Korolev, A. (2014). Mixed-phase clouds in a turbulent environment: Part 2: Analytic treatment. *Quarterly Journal of the Royal Meteorological Society*, 140, 870–880. https://doi.org/10.1256/qj.03.102

Field, P. R., Hogan, R. J., Brown, P. R. A., Illingworth, A. J., Choularton, T. W., Kaye, P. H., & Greenaway, R. (2004). Simultaneous radar and aircraft observations of mixed-phase cloud at the 100 m scale. *Quarterly Journal of the Royal Meteorological Society*, 130, 1877–1904. https://doi.org/10.1256/qj.03.102

Forbes, R. M., & Ahlgrimm, M. (2014). On the representation of high-latitude boundary layer mixed-phase cloud in the ECMWF global model. *Monthly Weather Review*, 142, 3425–3445. https://doi.org/10.1175/MWR-D-13-00325.1

Forbes, R. M., & Hogan, R. J. (2006). Observations of the depth of ice particle evaporation beneath frontal cloud to improve NWP modelling. *Quarterly Journal of the Royal Meteorological Society*, 132, 865–883. https://doi.org/10.1256/qj.04.187

Gilbert, E., Orr, A., King, J. C., Renfrew, I. A., Lachlan-Cope, T., Field, P. F., & Boutle, I. A. (2020). Summertime cloud phase strongly influences surface melting on the Larsen C ice shelf, Antarctica. *Quarterly Journal of the Royal Meteorological Society*, 146, 1575–1589. https://doi.org/10.1002/qj.3753

Hallett, J., & Mossop, S. C. (1974). Production of secondary ice particles during the riming process. *Nature*, 249, 26–28.

Haynes, J. M., Jakob, C., Rossow, W. B., Tselioudis, G., & Brown, J. (2011). Major characteristics of Southern Ocean cloud regimes and their effects on the energy budget. *Journal of Climate*, 24, 5061–5080. https://doi.org/10.1175/2011jcli4052.1

Hersbach, H., Bell, B., Berrisford, P., Hirahara, S., Horányi, A., Muñoz-Sabater, J., et al. (2020). The ERA5 Global Reanalysis. *Quarterly Journal of the Royal Meteorological Society*, 146, 1999–2049. https://doi.org/10.1002/qj.3803

Herzegh, P. H., & Hobbs, P. V. (1980). The mesoscale and microscale structure and organisation of clouds and precipitation in midlatitude cyclones. II: Warm frontal clouds. *Journal of the Atmospheric Sciences*, *37*, 597–611.

Heymsfield, A. J., Miloshevich, L. M., Slingo, A., Sassen, K., & Starr, D. O. (1991). An observational and theoretical study of highly super-cooled altocumulus. *Journal of the Atmospheric Sciences*, *48*, 923–945.

Hobbs, P. V., Matejka, T. J., Herzegh, P. H., Locatelli, J. D., & Houze, R. A. Jr. (1980). The mesoscale and microscale structure and organisa-tion of clouds and precipitation in midlatitude cyclones. I: A case study of a cold front. *Journal of the Atmospheric Sciences*, *37*, 568–596.

Hobbs, P. V., & Rangno, A. L. (1998). Microstructures of low and middle-level clouds over the Beaufort Sea. *Quarterly Journal of the Royal Meteorological Society*, *124*, 2035–2071.

Hogan, R. J., Francis, P. N., Flentje, H., Illingworth, A. J., Quante, M., & Pelon, J. (2003). Characteristics of mixed-phase clouds: Part I. Lidar, radar and aircraft observations from CLARE98. *Quarterly Journal of the Royal Meteorological Society*, *129*, 2089–2116.

Huang, Y., Franklin, C. N., Siems, S. T., Manton, M. J., Chubb, T., Lock, A., et al. (2015). Evaluation of boundary-layer cloud forecasts over the Southern Ocean in a limited-area numerical weather prediction system using in-situ, space-borne and ground-based observations. *Quarterly Journal of the Royal Meteorological Society*, *141*, 2259–2276. https://doi.org/10.1002/qj.2519

Huang, Y., Siems, S. T., Manton, M. J., Protat, A., & Delanoë, J. (2012). A study on the low-altitude clouds over the Southern Ocean using the DARDAR-MASK. *Journal of Geophysical Research*, *117*, D18204. https://doi.org/10.1029/2012JD017800

Huang, Y., Siems, S. T., Manton, M. J., & Thompson, G. (2014). An evaluation of WRF simulations of clouds over the Southern Ocean with ATrain observations. *Monthly Weather Review*, *142*, 647–667. https://doi.org/10.1175/MWR-D-13-00128.1

Hu, Y., Rodier, S., Xu, K., Sun, W., Huang, J., Lin, B., et al. (2010). Occurrence, liquid water content and fraction of supercooled wa-ter clouds from combined CALIOP/IIR/MODIS measurements. *Journal of Geophysical Research*, *115*, D00H34. https://doi.org/10.1029/2009JD012384

Jackson, R. C., McFarquhar, G. M., Korolev, A. V., Earle, M. E., Liu, P. S. K., Lawson, R. P., et al. (2012). The dependence of ice microphys-ics on aerosol concentration in Arctic mixed-phase stratus clouds during ISDAC and M-PACE. *Journal of Geophysical Research*, *117*, D15207. https://doi.org/10.1029/2012JD017668

Jullien, N., Vignon, E., Sprenger, M., Aemisegger, F., & Berne, A. (2020). Synoptic conditions and atmospheric moisture pathways asso-ciated with virga and precipitation over coastal Adélie Land in Antarctica. *The Cryosphere*, *14*, 1685–1702. https://doi.org/10.5194/tc-14-1685-2020

Kanitz, T., Seifert, P., Ansmann, A., Engelmann, R., Althausen, D., Casiccia, C., & Rohwer, E. G. (2011). Contrasting the impact of aer-osols at northern and southern midlatitudes on heterogeneous ice formation. *Geophysical Research Letters*, *38*, L17802. https://doi.org/10.1029/2011GL048532

Kay, J. E., Wall, C., Yettella, V., Medeiros, B., Hannay, C., Caldwell, P., & Bitz, C. (2016). Global climate impacts of fixing the South-ern Ocean shortwave radiation bias in the Community Earth System Model (CESM). *Journal of Climate*, *29*, 4617–4636. https://doi.org/10.1175/JCLI-D-15-0358.1

Keppas, S. C., Crosier, J., Choularton, T. W., & Bower, K. N. (2018). Microphysical properties and radar polarimetric features within a warm front. *Monthly Weather Review*, *146*, 2003–2022. https://doi.org/10.1175/MWR-D-18-0056.1

King, J. C., Gadian, A., Kirchgaessner, A., Kuipers Munneke, P., Lachlan-Cope, T. A., Orr, A., et al. (2015). Validation of the summertime surface energy budget of Larsen C Ice Shelf (Antarctica) as represented in three high-resolution atmospheric models. *Journal of Geo-physical Research: Atmospheres*, *120*, 1335–1347. https://doi.org/10.1002/2014JD022604

Klekociuk, A. R., French, W. J. R., Alexander, S. P., Kuma, P., & McDonald, A. J. (2020). The state of the atmosphere in the 2016 southern Kerguelen Axis campaign region. *Deep Sea Research II*, *174*, 104550. https://doi.org/10.1016/j.dsr2.2019.02.001

Kollias, P., Treserras, B. P., & Protat, A. (2019). Calibration of the 2007–2017 record of atmospheric radiation measurements cloud radar observations using CloudSat. *Atmospheric Measurement Techniques*, *12*, 4949–4964. https://doi.org/10.5194/amt-12-4949-2019

Korolev, A., & Field, P. R. (2008). The effect of dynamics on mixed-phase clouds: Theoretical considerations. *Journal of the Atmospheric Sciences*, *65*, 66–86. https://doi.org/10.1175/2007JAS2355.1

Korolev, A., Heckman, I., Wolde, M., Ackerman, A. S., Fridlind, A. M., Ladino, L. A., et al. (2020). A new look at the environmental conditions favourable to secondary ice production. *Atmospheric Chemistry and Physics*, *20*, 1391–1429. https://doi.org/10.5194/acp-20-1391-2020

Kuma, P., Mcdonald, A., Morgenstern, O., Alexander, S., Cassano, J., Garrett, S., et al. (2020). Evaluation of Southern Ocean cloud in the HadGEM3 general circulation model and MERRA-2 reanalysis using ship-based observations. *Atmospheric Chemistry and Physics*, *20*, 6607–6630. https://doi.org/10.5194/acp-20-6607-2020

Kumjian, M. R., Rutledge, S. A., Rasmussen, R. M., Kennedy, P. C., & Dixon, M. (2014). High-resolution polarimetric radar observations of snow-generating cells. *Journal of Applied Meteorology and Climatology*, *53*, 1636–1658. https://doi.org/10.1175/JAMC-D-13-0312.1

Lenaerts, J. T. M., Van Tricht, K., Lhermitte, S., & L'Ecuyer, T. S. (2017). Polar clouds and radiation in satellite observations, reanalyses and climate models. *Geophysical Research Letters*, *44*, 3355–3364. https://doi.org/10.1002/2016GL072242

Listowski, C., Delanoë, J., Kirchgaessner, A., Lachlan-Cope, T., & King, J. (2019). Antarctic clouds, supercooled liquid water and mixed-phase investigated with DARDAR: Geographical and seasonal variations. *Atmospheric Chemistry and Physics*, *19*, 6771–6808. https://doi.org/10.5194/acp-2018-1222

Luo, Y., Xu, K.-M., Morrison, H., McFarquhar, G. M., Wang, Z., & Zhang, G. (2008). Multi-layer arctic mixed-phase clouds simulated by a cloud-resolving model: Comparison with ARM observations and sensitivity experiments. *Journal of Geophysical Research*, *113*, D12208. https://doi.org/10.1029/2007JD009563

Mace, G. G. (2010). Cloud properties and radiative forcing over the maritime storm tracks for the Southern Ocean and North Atlantic derived from A-Train. *Journal of Geophysical Research*, *115*, D10201. https://doi.org/10.1029/2009JD012517

Mace, G. G., & Protat, A. (2018a). Clouds over the Southern Ocean as observed from the R/V Investigator during CAPRICORN. Part I: Cloud occurrence and phase partitioning. *Journal of Applied Meteorology and Climatology*, *57*, 1783–1803. https://doi.org/10.1175/JAMC-D-17-0194.1

Mace, G. G., & Protat, A. (2018b). Clouds over the Southern Ocean as observed from the R/V Investigator during CAPRICORN. Part II: The properties of non-precipitating stratocumulus. *Journal of Applied Meteorology and Climatology*, *57*, 1805–1823. https://doi.org/10.1175/JAMC-D-17-0195.1

Mace, G. G., Protat, A., Humphries, R. S., Alexander, S. P., McRobert, I. M., Ward, J., et al. (2021). Southern Ocean cloud properties derived from CAPRICORN and MARCUS data. *Journal of Geophysical Research: Atmospheres*, *126*, e2020JD033368. https://doi.org/10.1029/2020JD033368

Marchand, R., Ackerman, T., Smyth, M., & Rossow, W. B. (2009). A review of cloud top height and optical depth histograms from MISR, ISCCP, and MODIS. *Journal of Geophysical Research*, *115*, D16206. https://doi.org/10.1029/2009JD013422

Marchand, R., Ackerman, T., Westwater, E. R., Clough, S. A., Cady-Pereira, K., & Liljegren, J. C. (2003). An assessment of microwave absorption models and retrievals of cloud liquid water using clear-sky data. *Journal of Geophysical Research*, *108*(D24), 4773. https://doi.org/10.1029/2003JD003843

McCluskey, C. S., Hill, T. C. J., Humphries, R. S., Rauker, A. M., Moreau, S., Strutton, P. G., et al. (2018). Observations of ice nucleating particles over Southern Ocean waters. *Geophysical Research Letters*, *45*, 11989–11997. https://doi.org/10.1029/2018GL079981

McCoy, D. T., Hartmann, D. L., & Grosvenor, D. P. (2014). Observed Southern Ocean cloud properties and shortwave reflection. Part I: Calculation of SW flux from observed cloud properties. *Journal of Climate*, *27*, 8836–8857. https://doi.org/10.1175/JCLI-D-14-00287.1

McFarquhar, G. M., Bretherton, C., Marchand, R., Protat, A., DeMott, P. J., Alexander, S. P., et al. (2021). Observations of clouds, aerosols, precipitation and surface radiation over the Southern Ocean: An overview of CAPRICORN, MARCUS, MICRE and SOCRATES. *Bulletin of the American Meteorological Society*, 1–92. https://doi.org/10.1175/BAMS-D-20-0132.1

McFarquhar, G. M., Ghan, S., Verlinde, J., Korolev, A., Strapp, J. W., Schmid, B., et al. (2011). Indirect and semi-direct aerosol campaign: The impact of Arctic aerosols on clouds. *Bulletin of the American Meteorological Society*, *144*(92), 183–201. https://doi.org/10.1175/2010BAMS2935.1

McFarquhar, G. M., Zhang, G., Poellot, M. R., Kok, G. L., McCoy, R., Tooman, T., et al. (2007). Ice properties of single-layer stratocumulus during the Mixed-Phase Arctic Cloud Experiment: 1. Observations. *Journal of Geophysical Research*, *112*, D24201. https://doi.org/10.1029/2007JD008633

Mioche, G., Jourdan, O., Ceccaldi, M., & Delanoë, J. (2015). Variability of mixed-phase clouds in the Arctic with a focus on the Svalbard region: A study based on spaceborne active remote sensing. *Atmospheric Chemistry and Physics*, *15*, 2445–2461. https://doi.org/10.5194/acp-15-2445-2015

Morrison, A. E., Siems, S. T., & Manton, M. J. (2011). A three year climatology of cloudtop phase over the Southern Ocean and North Pacific. *Journal of Climate*, *24*, 2405–2418. https://doi.org/10.1175/2010JCLI3842.1

Morrison, H., de Boer, G., Feingold, G., Harrington, J., Shupe, M. D., & Sulia, K. (2012). Resilience of persistent Arctic mixed-phase clouds. *Nature Geoscience*, *5*, 11–17. https://doi.org/10.1038/NGEO1332

Noh, Y.-J., Miller, S. D., Heidinger, A. K., Mace, G., Protat, A., & Alexander, S. P. (2019). Satellite based detection of daytime supercooled liquid topped mixed-phase clouds over the Southern Ocean using the Advanced Himawari Imager. *Journal of Geophysical Research: Atmospheres*, *124*, 2677–2701. https://doi.org/10.1029/2018JD029524

Orr, A., Phillips, R., Webster, S., Elvidge, A., Weeks, M., Hosking, J. S., & Turner, J. (2014). Met Office Unified Model high resolution simulations of a strong wind event in Antarctica. *Quarterly Journal of the Royal Meteorological Society*, *140*, 2287–2297. https://doi.org/10.1002/qj.2296

Plummer, D. M., McFarquhar, G. M., Rauber, R. M., Jewett, B. F., & Leon, D. C. (2015). Microphysical properties of convectively generated fall streaks within the stratiform comma head region of continental winter cyclones. *Journal of the Atmospheric Sciences*, *72*, 2465–2483. https://doi.org/10.1175/JAS-D-14-0354.1

Protat, A., Schulz, E., Rikus, L., Sun, Z., Xiao, Y., & Keywood, M. (2017). Shipborne observations of the radiative effect of Southern Ocean clouds. *Journal of Geophysical Research: Atmospheres*, *121*, 318–328. https://doi.org/10.1002/2016JD026061

Rauber, R. M., Plummer, D. M., Macomber, M. K., Rosenow, A. A., McFarquhar, G. M., & Jewett, B. F. (2015). The role of cloud-top generating cells and boundary layer circulations in the finescale radar structure of a winter cyclone over the Great Lakes. *Monthly Weather Review*, *143*, 2291–2318. https://doi.org/10.1175/MWR-D-14-00350.1

Rauber, R. M., & Tokay, A. (1991). An explanation for the existence of supercooled water at the top of cold clouds. *Journal of the Atmospheric Sciences*, *48*, 1005–1023.

Rosenow, A. A., Plummer, D. M., Rauber, R. M., McFarquhar, G. M., Jewett, B. F., & Leon, D. (2014). Vertical velocity and physical structure of generating cells and convection in the comma head region of continental winter cyclones. *Journal of the Atmospheric Sciences*, *71*, 1538–1558. https://doi.org/10.1175/JASD130249

Sato, K., Inoue, J., Alexander, S. P., McFarquhar, G., & Yamazaki, A. (2018). Improved reanalysis and prediction of atmospheric fields over the Southern Ocean using campaign-based radiosonde observations. *Geophysical Research Letters*, *45*, 11406–11413. https://doi.org/10.1029/2018GL079037

Sotiropoulou, G., Sedlar, J., Forbes, R., & Tjernström (2016). Summer Arctic clouds in the ECMWF forecast model: And evaluation of cloud parameterisation schemes. *Quarterly Journal of the Royal Meteorological Society*, *142*, 387–400. https://doi.org/10.1002/qj.2658

Storelvmo, T., Tan, I., & Korolev, A. (2015). Cloud phase changes induced by CO_2 warming—A powerful yet poorly constrained cloud-climate feedback. *Current Climate Change Reports*, *1*, 288–296. https://doi.org/10.1007/s40641-015-0026-2

Tan, I., Storelvmo, T., & Zelinka, M. D. (2016). Observational constraints on mixed-phase clouds imply higher climate sensitivity. *Science*, *352*, 224–227. https://doi.org/10.1126/science.aad5300

Turner, J., Chenoli, S. N., Samah, A. A., Marshall, G., Phillips, T., & Orr, A. (2009). Strong wind events in the Antarctic. *Journal of Geophysical Research*, *114*, D18103. https://doi.org/10.1029/2008JD011642

Verlinde, J., Rambukkange, M. P., Clothiaux, E. E., McFarquhar, G. M., & Eloranta, E. W. (2013). Arctic multilayered, mixed-phase cloud processes revealed in millimeter-wave cloud radar Doppler spectra. *Journal of Geophysical Research: Atmospheres*, *118*, 13199–13213. https://doi.org/10.1002/2013JD020183

Vignon, E., Alexander, S. P., DeMott, P. J., Sotiropoulou, G., Gerber, F., Hill, T. C. J., & , et al. (2021). Challenging and improving the simulation of mid-level mixed-phase clouds over the high-latitude Southern Ocean. *Journal of Geophysical Research* (in press). https://doi.org/10.1029/2020JD033490

Vignon, E., Traullé, O., & Berne, A. (2019). On the fine vertical structure of the low troposphere over the coastal margins of East Antarctica. *Atmospheric Chemistry and Physics*, *19*, 4659–4683. https://doi.org/10.5194/acp-19-4659-2019

Wang, Y., McFarquhar, G. M., Rauber, R. M., Zhao, C., Wu, W., Finlon, J. A., et al. (2020). Microphysical properties of generating cells over the Southern Ocean: Results from SOCRATES. *Journal of Geophysical Research: Atmospheres*, *125*, e2019JD032237. https://doi.org/10.1029/2019JD032237

Wang, Z., & Sassen, K. (2001). Cloud type and macrophysical property retrieval using multiple remote sensors. *Journal of Applied Meteorology and Climatology*, *40*, 1665–1682. https://doi.org/10.1175/1520-0450(2001)040<1665:CTAMPR>2.0.CO;2

Young, G., Lachlan-Cope, T., O'Shea, S. J., Dearden, C., Listowski, C., Bower, K. N., & Gallagher, M. W. (2018). Radiative effects of secondary ice enhancement in coastal Antarctic clouds. *Geophysical Research Letters*, *46*, 2312–2321. https://doi.org/10.1029/2018GL080551